From donuts to drifting and beyond: controlling the nonlinear dynamics of automated vehicles

Yilun Zhang[a], Dénes Takács[b,c], and Gábor Orosz[a,d]

[a]Department of Mechanical Engineering, University of Michigan, Ann Arbor, MI 48109, USA
[b]Department of Applied Mechanics, Faculty of Mechanical Engineering, Budapest University of Technology and Economics, Budapest, H-1111, Hungary
[c]HUN-REN–BME Dynamics of Machines Research Group, Budapest, H-1111, Hungary
[d]Department of Civil and Environmental Engineering, University of Michigan, Ann Arbor, MI 48109, USA

ARTICLE HISTORY
Compiled July 16, 2025

ABSTRACT
The nonlinear dynamics of automated vehicles are studied. A 5 degree-of-freedom single track model is derived using the Appellian approach to describe the dynamics of rear-wheel drive and front-wheel steer automobiles. This model captures the interactions between the vehicle body and the wheels while eliminating the calculation of the internal reaction forces and torques. An anisotropic combined slip brush tire model is constructed to describe tire characteristics. The handling characteristics are analyzed by using bifurcation analysis: stable and unstable invariant solutions are studied while varying the steering angle and driving torque. The results provide insights about the existence and stability of steady states (namely, steady state cornering, donut, drifting) and periodic orbits, and this knowledge is utilized when designing simple, computationally inexpensive controllers that can stabilize unstable states and navigate the system between them. This establishes a flexible control framework that can be used to realize a large variety of extreme maneuvers.

KEYWORDS
5 DoF Single Track Model; Combined Slip Brush Tire Model; Bifurcation Analysis; Vehicle Handling; Controlling Extreme Maneuvers

1. Introduction

Vehicle automation has been receiving increasing attention in various research communities [1]. The majority of efforts in understanding handling dynamics and controller development focused on mild handling maneuvers such as lane keeping and lane changing, which have made their ways to driving assistance systems deployed on production vehicles with lower levels of automation. However, for higher levels of automation, vehicle control systems should be able to execute more extreme maneuvers in order to be deployed without requiring human takeover while ensuring safety.

During the last decade, the idea of studying the dynamics of race car drivers and utilizing this knowledge to drive vehicles at the handling limit rose to prominence in the literature [2–4]. A variety of control techniques have been deployed to mimic the

Email: yilunz@umich.edu, takacs@mm.bme.hu, orosz@umich.edu

capabilities of expert human drivers, and most of them rely on some optimization technique. For example, in [5] a backstepping controller was utilized to generate torque input to track the wheel speed obtained using a linear quadratic regulator (LQR). Model predictive control (MPC), i.e., rolling horizon optimal control, has often been utilized to control the dynamics close to the handling limits [6,7]. In particular, initiating and stabilizing drifting (a steady state when the vehicle is turning to the opposite direction than suggested by the steering angle) has generated interest in the community. Apart from theoretical works [8,9], autonomous drifting has recently been realized experimentally using real vehicles [10–14].

There has been substantial effort in trying to understand the nonlinear dynamics of vehicle handling. In particular, using phase portraits (in the plane of lateral velocity and yaw rate for fixed values of longitudinal velocity and steering angle) was proven to be very informative. This allows one to map out the different equilibria and the dynamics around them, i.e., determine whether they are stable, unstable or saddle type [7,15,16]. Apart from equilibria, one may also study stable and unstable limit cycle oscillations (periodic orbits) [17–19]. For models where the longitudinal dynamics is considered as a state, the phase portraits become three-dimensional [20,21], but analysis may be executed similarly. In addition, one may study the qualitative changes of equilibria and periodic solutions when varying the parameters (e.g., the steering angle and the longitudinal velocity) and detect bifurcation points where different branches meet and change their stability [18,22,23]. Such analysis was even proven to be useful for understanding the ground handling of aeroplanes [24].

The above dynamic models typically only consider the lateral tire deformation captured by physics-based models like the brush model [25–27], or by data-based models like the magic formula [28] and neural networks [29]. To improve accuracy, combined slip models, which take into account both the longitudinal and lateral tire deformations and include the wheel rotations, have been utilized [12,13,30–34]. Inspired by these results, in this paper we construct a single track vehicle model that incorporates the longitudinal, lateral and yaw dynamics of the vehicle body as well as the wheel dynamics. We utilize the Appellian approach [35–42] to accurately capture the multi-body interactions, while eliminating the calculation of the internal reaction forces and torques acting between the bodies. This 5 degree-of-freedom (DoF) model is equipped with a combined slip tire model with the following novelties: (i) it takes into account the anisotropic property of the tires as it incorporates the longitudinal and lateral stiffnesses; (ii) it differentiates the static and sliding friction coefficients enabling non-monotonic force characteristics; (iii) it can handle negative wheel speed which is becoming important for electric vehicles; (iv) it takes into account the aligning moments.

The nonlinear dynamics of the constructed 5 DoF model is analyzed using bifurcation analysis, namely, the numerical continuation software DDE-biftool [43,44]. Different steady states (steady state cornering, donut, and drifting) are identified and continued when varying the constant driving torque and the constant steering angle. The behavior around the different steady states is visualized using phase portraits and by depicting the motion of the vehicle in the physical space. Through bifurcations along the branches of steady states, periodic solutions are detected and analyzed in state space and in physical space. These results shed light on how the invariant solutions connect to each other and reveal which solutions are realizable depending on the driving inputs. The detailed knowledge of the state space dynamics of the uncontrolled system enables us to design simple, computationally inexpensive controllers that can stabilize unstable donut and drifting states. In particular, as opposed to nonlinear

MPC, we utilize a linear quadratic regulator (LQR) based control design, which results in explicit state feedback controllers. We demonstrate that by switching between the controllers, the vehicle may realize a plethora of different emergency maneuvers.

The rest of the paper is organized as follows. In Section 2, we summarize the behavior of the traditional single track model. Our 5 DoF model, together with the combined slip brush tire model, is presented in Section 3. The bifurcation analysis of steady states and periodic solutions is carried out in Section 4, while the control design to stabilize the unstable handling solutions is presented in Section 5. Finally, we conclude our results and point out our future research directions in Section 6.

2. Traditional single track model of vehicle dynamics

In this section, we provide a brief summary of the dynamics of a so-called traditional single track model which is widely used in the literature. We highlight the different solutions (steady-state cornering, donut, drifting) and show how these change as the longitudinal velocity is increased. We also highlight the shortcomings of the traditional model regarding the simplification of the dynamics and the inability to accommodate the control design of different motions.

2.1. Governing equations

The mechanical model is shown Figure 1. The front wheels are merged as a single wheel and the rear wheels are also merged as a single wheel. The centers R and F of the rear and front wheels are separated by the wheelbase l. The distance between the center of gravity G and the rear wheel center R is denoted by d. The distance between the center of gravity G and the front wheel center F is denoted by q. Indeed, $d + q = l$. The mass of the vehicle is m and its mass moment of inertia with respect to z-axis at the center of gravity G is J_{G}. The location and orientation of the vehicle is described by the position of the center of mass $(x_{\mathrm{G}}, y_{\mathrm{G}})$ and the yaw angle ψ in the Earth-fixed frame F_0 while the velocity state is described by the longitudinal velocity v, the lateral velocity σ of the center of gravity and the yaw rate ω. The longitudinal velocity v is considered to be a constant parameter. This corresponds to a kinematic constraint of keeping the rotational speed of the rear wheel constant (which implicitly assumes a rear wheel drive vehicle). The remaining quantities $\sigma, \omega, \psi, x_{\mathrm{G}}, y_{\mathrm{G}}$ are used as the time-varying states of the dynamic system, while the steering angle γ is a time-varying input. The equations of motion can be found for example in [18]:

$$\begin{aligned}
\dot{\sigma} &= -v\omega + \frac{1}{m}\big(F_{y,\mathrm{r}} + F_{y,\mathrm{f}}\cos\gamma\big), \\
\dot{\omega} &= \frac{1}{J_{\mathrm{G}}}\big(-F_{y,\mathrm{r}}d + F_{y,\mathrm{f}}q\cos\gamma + M_{z,\mathrm{r}} + M_{z,\mathrm{f}}\big), \\
\dot{\psi} &= \omega, \\
\dot{x}_{\mathrm{G}} &= v\cos\psi - \sigma\sin\psi, \\
\dot{y}_{\mathrm{G}} &= v\sin\psi + \sigma\cos\psi.
\end{aligned} \tag{1}$$

Here the tire lateral forces $F_{y,\mathrm{r}}(\alpha_{\mathrm{r}})$, $F_{y,\mathrm{f}}(\alpha_{\mathrm{f}})$ and the tire self-aligning moments

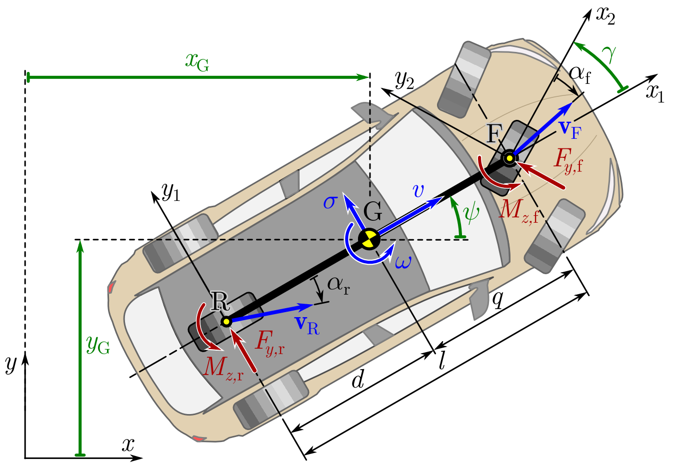

Figure 1. Traditional single track model which takes into account the lateral deformation of the tires. The coordinate frames, the geometric and kinematic quantities, the lateral tire forces and the aligning moments are shown in the figure.

$M_{z,\mathrm{r}}(\alpha_{\mathrm{r}})$, $M_{z,\mathrm{f}}(\alpha_{\mathrm{f}})$ are determined by means of the tire slip angles

$$\begin{aligned}\alpha_{\mathrm{r}} &= -\arctan\left(\frac{\sigma - d\omega}{v}\right) . \\ \alpha_{\mathrm{f}} &= \gamma - \arctan\left(\frac{\sigma + q\omega}{v}\right) ,\end{aligned} \tag{2}$$

and the normal forces

$$\begin{aligned}F_{z,\mathrm{f}} &= \frac{mgd}{l} , \\ F_{z,\mathrm{r}} &= \frac{mgq}{l} ,\end{aligned} \tag{3}$$

where we considered the static weight distribution for simplicity.

The tire force and self-aligning moment characteristics can be based on different tire models [25,28]. Here, for the sake of simplicity, we use the brush tire model [23,27,45]:

$$\begin{aligned}F_y(\alpha) &= \begin{cases}\phi_1 \tan\alpha + \phi_2 \,\mathrm{sgn}\,\alpha \tan^2\alpha + \phi_3 \tan^3\alpha, & \text{if } \ |\alpha| \le \alpha_{\mathrm{cr}}, \\ \mu F_z \mathrm{sgn}\,\alpha, & \text{if } \ |\alpha| > \alpha_{\mathrm{cr}},\end{cases} \\ M_z(\alpha) &= \begin{cases}\mu_1 \tan\alpha + \mu_2 \,\mathrm{sgn}\,\alpha \tan^2\alpha + \mu_3 \tan^3\alpha + \mu_4 \,\mathrm{sgn}\,\alpha \tan^4\alpha, & \text{if } \ |\alpha| \le \alpha_{\mathrm{cr}}, \\ 0, & \text{if } \ |\alpha| > \alpha_{\mathrm{cr}},\end{cases}\end{aligned} \tag{4}$$

where

$$\begin{aligned}&\phi_1 = 2k_y a^2, \quad \phi_2 = -\frac{(2k_y a^2)^2}{3\mu_0 F_z}\left(2 - \frac{\mu}{\mu_0}\right), \quad \phi_3 = \frac{(2k_y a^2)^3}{(3\mu_0 F_z)^2}\left(1 - \frac{2\mu}{3\mu_0}\right), \\ &\mu_1 = -\frac{a}{3}\phi_1, \quad \mu_2 = -a\phi_2, \quad \mu_3 = -3a\phi_3, \quad \mu_4 = a\frac{(2k_y a^2)^4}{(3\mu_0 F_z)^3}\left(\frac{4}{3} - \frac{\mu}{\mu_0}\right),\end{aligned} \tag{5}$$

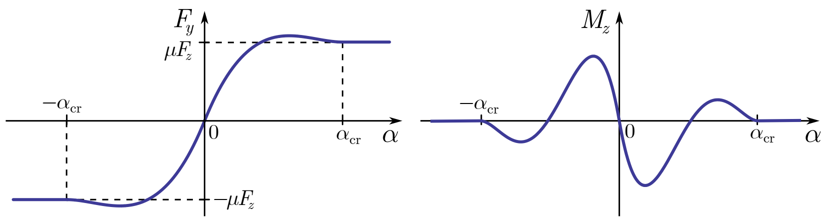

Figure 2. Lateral tire force F_y and aligning torque M_z characteristics as the function of the tire slip angle α.

see Figure 2. Here a is the half-length of the tire-ground contact patch, k_y is the lateral stiffness per unit length of the tires, F_z is the normal force acting on the tire, μ and μ_0 are the friction coefficients between the tire and the road for sliding and rolling, respectively. The critical side-slip angle $\alpha_{\rm cr} = \arctan \frac{3\mu_0 F_z}{2k_y a^2}$ corresponds to the condition at which the sliding region expands to the whole contact patch while the constant $C_y := 2k_y a^2$ is often referred to as the cornering stiffness.

We remark that the nonlinear system (1)–(5) consist of five first order differential equations, and considering that one degree of freedom (DoF) in mechanics correspond to two first order differential equations, the model is often referred to as a 2.5 DoF single track model of rear wheel drive automobiles. Also note that, the equations in (1) are ordered such that the system can be separated into essential dynamics (the two equations) and hidden dynamics (the second three equations) such that the essential dynamics is independent of the hidden dynamics. Thus, when analyzing the dynamics one may focus on the first two equations. However, when designing controllers for automated vehicles the position variable are also often used in the feedback laws leading to a fully coupled system.

2.2. Steady-state solutions and stability

As mentioned above, in the traditional single track model the longitudinal velocity is a constant parameter $v(t) = v^*$. In order to analyze the steady state solutions we also consider the steering angle input to be constant $\gamma(t) = \gamma^*$. Then one may analyze the dynamics of the corresponding autonomous dynamical system. In particular, we may find the steady state solutions $\sigma(t) = \sigma^*$, $\omega(t) = \omega^*$ using the first two equations in (1). These solutions correspond to circular motion of radius $\rho_{\rm G} = \sqrt{(v^*)^2 + (\sigma^*)^2}/\omega^*$ which can be derived form the last three equations in (1); see [18]. The software package MDBM [46] can be utilized to find the steady states and then these can be continued as the parameters are varied using the software package DDE-Biftool [43,44], which can also compute the linear stability of steady states.

Figure 3(a,b) show the steady state solutions as a function of the longitudinal velocity v for the constant steering input $\gamma = 10°$. The other parameters are taken from Table 1 such that $m = m_{\rm v} + 2m_{\rm w}$. Green and red colors refer to stable and unstable solutions, respectively. The stable branch correspond to steady state cornering which is characterized by small lateral velocity and yaw rate. The solid unstable branches meet at the fold point (marked by blue triangle). These correspond to donuts, that is, circular motions which exhibit positive yaw rate for positive steering angle. Notice that donuts are not possible for higher speeds. The dashed unstable branches are drifting solutions which are characterized by negative yaw rate for positive steering angle. We emphasize that donuts and drifting differ in the sign of the yaw rate and, as shown in the figure, in their turning radius too.

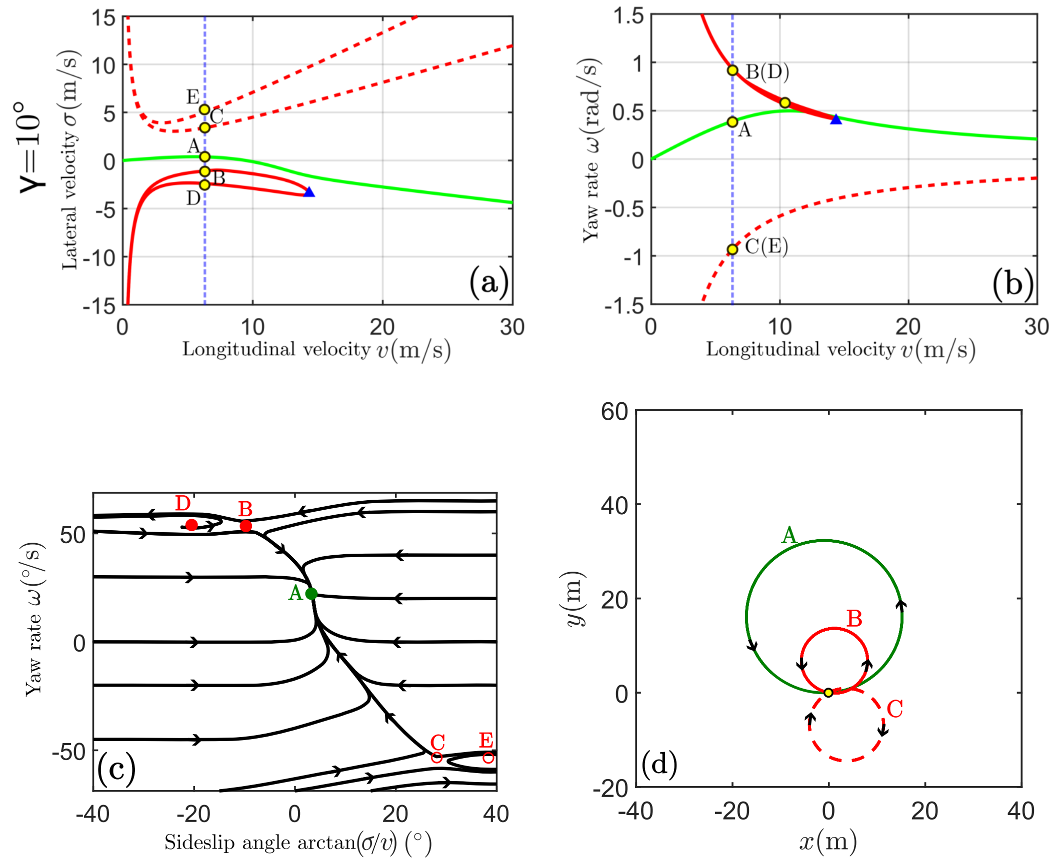

Figure 3. Dynamics of the traditional single track model for steering angle $\gamma = 10°$. (a,b) Bifurcation diagrams while using the longitudinal velocity as the bifurcation parameter. Stable and unstable solutions are shown by green an red curves: steady state cornering (solid green), donut (solid red), drifting (dashed red). (c) State space picture highlighting the different steady-state solutions for longitudinal velocity $v = 6.3\,\mathrm{m/s}$: steady state cornering (green dot), donut (red dot), drifting (red cirle). (d) Trajectories traced by the center of gravity G : steady state cornering (solid green circle), donut (solid red circle), drifting (dashed red circle).

In order to visualize the dynamics around different steady states and the connections between them, Figure 3(c) depicts the steady states and the trajectories in state space for longitudinal velocity $v = 6.3\,\mathrm{m/s}$; cf. blue dotted line in panels (a) and (b). Here beside the yaw rate ω we use the sideslip angle $\arctan(\sigma/v)$ at the center of gravity G. The same color code is used as in panels (a) and (b), that is, the green dot denotes the stable steady state cornering (A) while the unstable donut (B,D) and unstable drifting (C,E) solutions are marked by red dots and red circles, respectively. The state space picture also highlights the difference between the two donut solutions B and D: while solution B is a saddle, solution D is an unstable focus. Similarly, the drifting solution C is a saddle and the drifting solution E is an unstable focus. The stable manifolds of the saddle states B and C constitute the boundaries of the basin of attraction of the (locally) stable steady state cornering A. Note that sufficiently large perturbations may put the system outside of basin and make the system diverge from the (only locally) stable equilibrium.

The traces of the center of mass G in are shown in Figure 3(d) for the steady state solutions A, B and C. These are obtained by substituting the steady state solutions into the last three equations of (1). One may observe that stable steady state cornering solution A (solid green circle) has much larger radius compared to the donut solution B (solid red circle) and drifting solution C (dashed red circle). Also, in cases A and B the vehicle is moving counterclockwise corresponding to the positive steering angle while in case C it is moving clockwise (despite the positive steering angle). We remark that solutions D and E correspond very large tire slip angles which may not be realized in practice so these are not depicted in panel (d). The existence of these solutions in fact shows the limitation of the traditional single track model.

One may also notice in Figure 3(a) and (b) that the steady state cornering solution exists even for very large longitudinal velocities, which is also unrealistic in practice. This results from the fact the kinematic constraint of constant longitudinal velocity used in the traditional model eliminates the longitudinal dynamics and assumes that the longitudinal tire forces are as large as needed to maintain the constraint. Finally, while drivers typically stabilize donuts and drifting by controlling the torque applied at the rear wheel and the steering angle set for the front wheel, the traditional model only possesses the latter as control input, which makes control design, that aims to stabilize the unstable motions, unfeasible. These shortcomings motivate us to develop a higher fidelity vehicle model where the longitudinal dynamics of the vehicle as well as the longitudinal dynamics of the tires are taken into account. The detailed investigation of this model reveals a plethora of physically realistic solutions, which can be observed in practice. Additionally, a model includes the driving torque as input, enabling us to design controllers for different solutions.

3. Modeling

Motivated by the shortcomings of the traditional 2.5 DoF single track model, here we construct a higher-fidelity 5 DoF single track model, which incorporates the longitudinal dynamics of the automobile as well as the masses and mass moments of inertia of the wheels. We utilize the Appellian approach to capture the interactions between the vehicle body and the wheels, while eliminating the calculation of the internal reaction forces and reaction torques in the multi-body system. This is supported by an anisotropic combined slip tire model, which incorporates both the lateral and the longitudinal tire deformations while accurately representing the differences in the longitudinal and lateral stiffnesses and the differences in the static and sliding friction coefficients. Moreover, the model is also valid for negative wheel speed, which is becoming more important for electric vehicles with independent wheel drives. We also show that once the longitudinal and wheel dynamics are neglected, the higher fidelity model degrades to the traditional model.

3.1. 5 DoF Single Track Model

Here we present a single track model intended to capture the nonlinear handling dynamics of a rear-wheel drive, front-wheel steer automobile. In the main text we only introduce the notations and terminologies that are essential to understand the model and which will be used in the forthcoming analysis. The detailed derivation process using the Appellian approach is available in Appendix A for the interested readers. In addition, the differences and potential advantages of this 5 DoF model are highlighted and compared to the traditional 2.5 DoF model introduced in the previous section.

Figure 4 shows the mechanical model representing a multi-body system with three rigid bodies: vehicle body, rear axle (modeled as a single rear wheel), and front axle

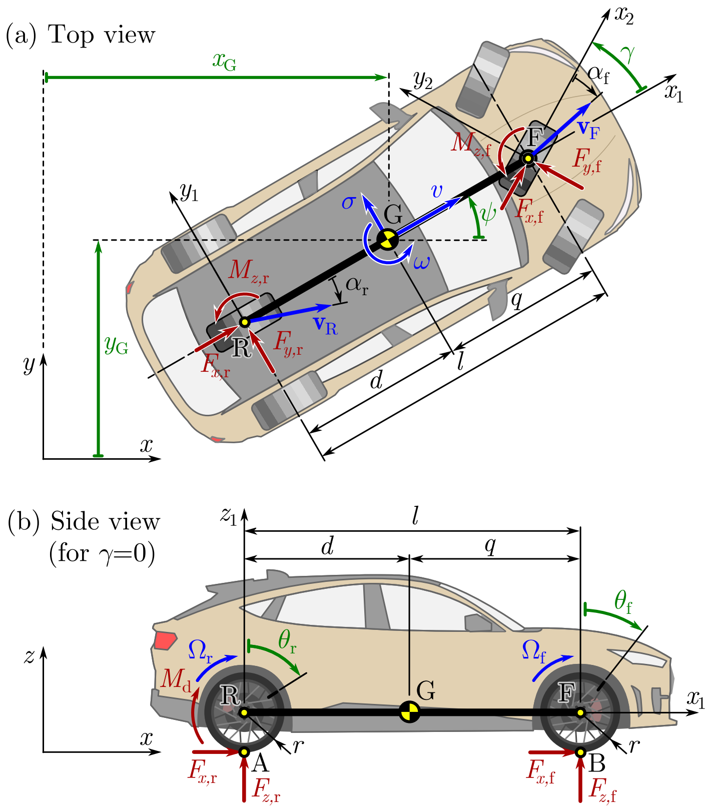

Figure 4. Higher fidelity single track model which takes into account both the lateral and the longitudinal deformation of the tires. The coordinate frames, the geometric and kinematic quantities, the longitudinal and lateral tire forces, and the aligning moments are shown in the figure.

(modeled as a single front wheel). Three coordinate frames are defined: (x, y, z) is fixed to the ground, (x_1, y_1, z_1) is fixed to the rear axle, and (x_2, y_2, z_2) is fixed to the front axle. The directions x_1, y_1, and $z = z_1 = z_2$ are referred to as longitudinal, lateral and vertical. From the side view, one can see that the center of mass is assumed to be at the same height as wheel centers. This assumption is reasonable in case of electric vehicles that generally have low center of gravity due to the heavy battery packs embedded in the bottom of the chassis. As a result, the pitch and roll motion as well as the effect of acceleration on the longitudinal weight transfer are ignored. The vehicle parameters including the dimensions as well as the mass and inertia terms are given in Table 1.

Five configuration coordinates are needed to describe the vehicle. Here we chose the position (x_G, y_G) of the center of mass G in the ground-fixed coordinate frame, the yaw angle ψ, and the rotation angles θ_R and θ_F of the rear wheel and the front wheel, respectively. Since there are no kinematic constraints, five velocity states are needed. We use the longitudinal velocity v and the lateral velocity σ of the center of mass G, the yaw rate ω, and the rotational speeds Ω_r and Ω_f of the rear wheel and the front wheel, respectively. Finally, the vehicle has two control inputs: the driving torque M_d and the steering angle γ.

First, the kinematic relationships between the derivatives of the configuration coordinates (generalized velocities) and the defined velocity states (pseudo velocities) are derived yielding the differential equations:

$$\begin{aligned}
\dot{x}_{\mathrm{G}} &= v\cos\psi - \sigma\sin\psi,\\
\dot{y}_{\mathrm{G}} &= v\sin\psi + \sigma\cos\psi,\\
\dot{\psi} &= \omega,\\
\dot{\theta}_{\mathrm{r}} &= \Omega_{\mathrm{r}},\\
\dot{\theta}_{\mathrm{f}} &= \Omega_{\mathrm{f}}.
\end{aligned}\tag{6}$$

The differential equations for the five velocity states are then derived following the Appellian approach:

$$\begin{aligned}
\dot{v} &= \sigma\omega + \frac{1}{m}\big(p\omega^2 + F_{x,\mathrm{r}} + F_{x,\mathrm{f}}\cos\gamma - F_{y,\mathrm{f}}\sin\gamma\big),\\
\dot{\sigma} &= -v\omega + \frac{1}{Jm-p^2}\big((J+pd)F_{y,\mathrm{r}} + (J-pq)(F_{x,\mathrm{f}}\sin\gamma + F_{y,\mathrm{f}}\cos\gamma)\\
&\qquad\qquad - p(M_{z,\mathrm{r}} + M_{z,\mathrm{f}} - C\ddot{\gamma})\big),\\
\dot{\omega} &= \frac{1}{Jm-p^2}\big(-(md+p)F_{y,\mathrm{r}} + (mq-p)(F_{x,\mathrm{f}}\sin\gamma + F_{y,\mathrm{f}}\cos\gamma)\\
&\qquad\qquad + m(M_{z,\mathrm{r}} + M_{z,\mathrm{f}} - C\ddot{\gamma})\big),\\
\dot{\Omega}_{\mathrm{r}} &= \frac{1}{D}(M_{\mathrm{d}} - rF_{x,\mathrm{r}}),\\
\dot{\Omega}_{\mathrm{f}} &= \frac{1}{D}(-rF_{x,\mathrm{f}}),
\end{aligned}\tag{7}$$

where

$$\begin{aligned}
m &= m_{\mathrm{v}} + 2m_{\mathrm{w}},\\
p &= m_{\mathrm{w}}(q-d),\\
J &= J_{\mathrm{G}} + m_{\mathrm{w}}\big(d^2+q^2\big) + 2C.
\end{aligned}\tag{8}$$

The longitudinal tire forces $F_{x,\mathrm{r}}$, $F_{x,\mathrm{f}}$, the lateral tire forces $F_{y,\mathrm{r}}$, $F_{y,\mathrm{f}}$, and the aligning moments $M_{z,\mathrm{r}}$, $M_{z,\mathrm{f}}$ appear in the differential equations (7). These arise from the tire elasticity and the tire-road friction and will be captured by a combined slip brush tire model explained in detail in Section 3.2. Observe that the 5 DoF single track model consists of two parts: the so-called essential dynamics (7) and the latent dynamics (6). When the control inputs M_{d} and γ do not depend on the configuration coordinates, the essential dynamics (7) can be solved on its own and the solution feeds into the latent dynamics (6). However, when using feedback laws which depend on the configuration coordinates (e.g., to navigate around objects), then the system (6)-(7) becomes fully connected. Admittedly, the last two equations in (6) have little practical meaning since the wheel rotation angles θ_{r} and θ_{f} are not of interest in most cases. These two equations are presented here for completeness.

In conclusion, the 5 DoF single track model presented here is an extension of traditional 2.5 DoF single track model by adding the longitudinal dynamics and treating the front and rear wheels as rigid bodies with mass and inertia. This leads to modified coefficients and additional terms in the first three equations of (7), (8), cf. the first two equations of (1). Including the rotational speeds of the front and rear wheels as sys-

Table 1. Vehicle Model Specifications

	Parameter	Value	Unit
m_{v}	Vehicle body mass	1200	kg
m_{w}	Front and rear wheel mass	100	kg
J_{G}	Vehicle mass moment of inertia about the z axis	2500	$\mathrm{kg} \cdot \mathrm{m}^2$
C	Wheel mass moment of inertia about the z axis	2.77	$\mathrm{kg} \cdot \mathrm{m}^2$
D	Wheel mass moment of inertia about the y_1 and y_2 axes	4.5	$\mathrm{kg} \cdot \mathrm{m}^2$
l	Wheelbase	2.5	m
d	Distance between the center of mass and the rear axle	1.5	m
q	Distance between the center of mass and the front axle	1	m
r	Effective wheel radius	0.3	m
k_x	Tire longitudinal stiffness per unit length	$4 \cdot 10^6$	$\mathrm{N/m}^2$
k_y	Tire lateral stiffness per unit length	$2 \cdot 10^6$	$\mathrm{N/m}^2$
a	Half contact patch length	0.1	m
μ_0	Static friction coefficient	0.9	
μ	Sliding friction coefficient	0.6	

tem states makes it possible to use a combined slip brush tire model with longitudinal and lateral slip terms capturing the tire-road interaction as described in Section 3.2. Also, the accelerator/brake input is assigned by the driving torque control input instead of by the longitudinal velocity (or by an imaginary driving force). This enables us to directly investigate the effect of pedal input on system dynamics, as shown in Sections 4.2 and 4.3, which is particularly important in extreme handling scenarios (including donut and drifting), where the vehicle motion is controlled by both steering and pedal inputs. In addition, as the penetration of electrification in consumer vehicles is rapidly increasing, using driving torque as input is gaining more practical meaning since controlling torque of electric motors is more direct compared to internal combustion engines.

3.2. Combined slip Brush Tire Model

Here we construct a combined slip brush tire model to calculate the longitudinal tire forces $F_{x,\mathrm{r}}$, $F_{x,\mathrm{f}}$, the lateral tire forces $F_{y,\mathrm{r}}$, $F_{y,\mathrm{f}}$, and the aligning moments $M_{z,\mathrm{r}}$, $M_{z,\mathrm{f}}$ appearing in (7). This in turn determines how the longitudinal velocity v, the lateral velocity σ, the yaw rate ω and the wheel speeds Ω_{f} and Ω_{r} change in time while commanding the steering angle γ and the driving torque M_{d}. The combined slip tire model developed here derives the forces and torques from the tire elasticity and road friction for anisotropic tires. This generalizes prior isotropic models in the literature [12,13,17,32,33] developed based on the Fiala model [25] or Pacejka's magic formula [28]. The new tire model also explicitly differentiates the sliding and sticking friction coefficients, allowing force characteristics that do not increase monotonically with the slips but rather have distinct maxima. Beyond the longitudinal and lateral force components the tire model also captures the aligning moments which may influence the steering dynamics. Finally, through appropriate definitions of slips, our tire model can accommodate negative wheel speed.

The key characteristics of the brush tire model are shown in Figure 5, where the

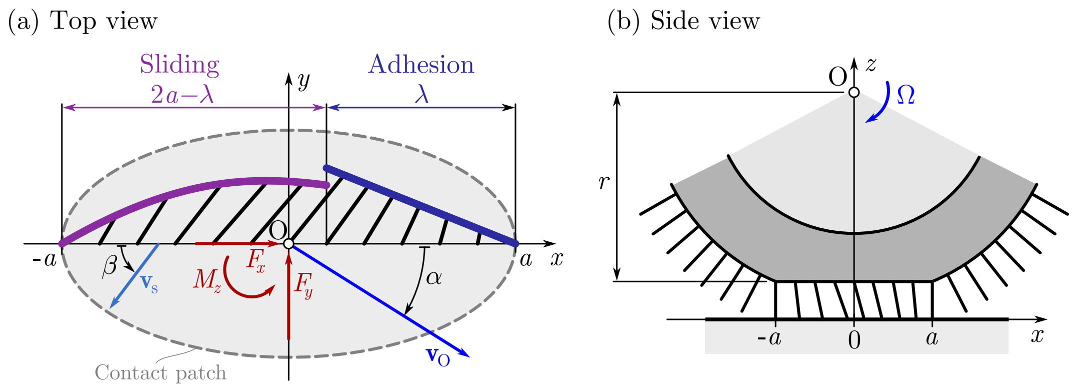

Figure 5. Combined slip brush tire model highlighting the adhesion region and the sliding region and indicating the slip angle α and the sliding angle β. The longitudinal and lateral tire forces F_x and F_y, and the aligning moment M_z are also shown on the figure.

wheel center is denoted by O (taking the role of R for the rear wheel and F for the front wheel). The coordinate frame (x, y, z) is aligned with the wheel and travels with the wheel. This corresponds to the coordinate frame (x_1, y_1, z_1) for the rear wheel and to the coordinate frame (x_2, y_2, z_2) for the front wheel in Figure 4. It is assumed that the tire consists of an unstretchable band with (infinitesimally small) brush-like elements attached to it. These brushes can deform both in the longitudinal and lateral directions along the contact patch (where the tire is in contact with the road surface). The longitudinal stiffness per unit length is k_x, the lateral stiffness per unit length is k_y, the length of the contact patch is $2a$, and the effective radius of the wheel is r; see Table 1 for the numerical values of these parameters. The resultant longitudinal and lateral forces F_x and F_y act at the center of the contact patch, while the asymmetry of the force distribution is captured by the aligning moment M_z. These force and moment components also depend on the static friction coefficient μ_0 and the sliding friction coefficient μ (see Table 1) as well as on the velocity $\mathbf{v}_{\mathrm{O}}$ of the wheel center O and the rotational velocity Ω of the wheel.

The velocity $\mathbf{v}_{\mathrm{O}}$ of the wheel center is not aligned with the wheel plane but forms the slip angle α. At the same time there is a mismatch between the wheel directional component $v_{\mathrm{O}} \cos\alpha$ and $r\Omega$, where we used the notation $|\mathbf{v}_{\mathrm{O}}| = v_{\mathrm{O}} > 0$. In order to quantify these mismatches we define the longitudinal slip and the lateral slip as

$$
\begin{aligned}
S_x &= \frac{r\Omega - v_{\mathrm{O},x}}{|r\Omega|} = \frac{r\Omega - v_{\mathrm{O}} \cos\alpha}{|r\Omega|}, \\
S_y &= -\frac{v_{\mathrm{O},y}}{|r\Omega|} = \frac{v_{\mathrm{O}} \sin\alpha}{|r\Omega|},
\end{aligned} \tag{9}
$$

where the absolute value is enforced in the denominator to accommodate negative wheel speeds. In addition, the negative sign in the definition of the lateral slip S_y corresponds to the definition of the slip angle in Figure 5(a): positive slip angle corresponds to positive lateral deformation at the front part of the contact patch, which yields positive lateral force.

In order to calculate the slip terms for the rear wheel and the front wheel in the 5 DoF single track model, we need to calculate the velocities of the wheel center points R and F. For the rear wheel, using the transport formula and resolving the vectors in the (x_1, y_1, z_1) coordinate frame (denoted as F_1), we obtain

$$\mathbf{v}_{\mathrm{R}} = \mathbf{v}_{\mathrm{G}} + \boldsymbol{\omega}_{\mathrm{v}} \times \mathbf{r}_{\mathrm{GR}} = \begin{bmatrix} v \\ \sigma - d\omega \\ 0 \end{bmatrix}_{\mathrm{F}_1} , \tag{10}$$

which leads to

$$\begin{aligned} S_{x,\mathrm{r}} &= \frac{r\Omega_{\mathrm{r}} - v}{|r\Omega_{\mathrm{r}}|} , \\ S_{y,\mathrm{r}} &= \frac{-\sigma + d\omega}{|r\Omega_{\mathrm{r}}|} . \end{aligned} \tag{11}$$

Here, $\mathbf{v}_{\mathrm{G}} = [\, v \quad \sigma \quad 0\,]_{\mathrm{F}_1}^{\top}$ denotes the velocity vector of the center of mass of the vehicle, $\boldsymbol{\omega}_{\mathrm{v}} = [\,0 \ \ 0 \ \ \omega\,]_{\mathrm{F}_1}^{\top}$ denotes the angular velocity vector of the vehicle body, while $\mathbf{r}_{\mathrm{GR}} = [\,-d \ \ 0 \ \ 0\,]_{\mathrm{F}_1}^{\top}$ denotes the position vector pointing from G to R.

Similarly, for the front wheel, resolving the vectors in the (x_2, y_2, z_2) coordinate frame (denoted as F_2), we obtain

$$\mathbf{v}_{\mathrm{F}} = \mathbf{v}_{\mathrm{G}} + \boldsymbol{\omega}_{\mathrm{v}} \times \mathbf{r}_{\mathrm{GF}} = \begin{bmatrix} v\cos\gamma + (\sigma + q\omega)\sin\gamma \\ -v\sin\gamma + (\sigma + q\omega)\cos\gamma \\ 0 \end{bmatrix}_{\mathrm{F}_2} , \tag{12}$$

which leads to

$$\begin{aligned} S_{x,\mathrm{f}} &= \frac{r\Omega_{\mathrm{f}} - v\cos\gamma - (\sigma + q\omega)\sin\gamma}{|r\Omega_{\mathrm{f}}|} , \\ S_{y,\mathrm{f}} &= \frac{v\sin\gamma - (\sigma + q\omega)\cos\gamma}{|r\Omega_{\mathrm{f}}|} . \end{aligned} \tag{13}$$

Here, we used the velocity vector $\mathbf{v}_{\mathrm{G}} = [\, v\cos\gamma + \sigma\sin\gamma \quad -v\sin\gamma + \sigma\cos\gamma \ \ 0\,]_{\mathrm{F}_2}^{\top}$, the angular velocity vector $\boldsymbol{\omega}_{\mathrm{v}} = [\,0 \ \ 0 \ \ \omega\,]_{\mathrm{F}_2}^{\top}$, and the position vector $\mathbf{r}_{\mathrm{GF}} = [\, q\cos\gamma \quad -q\sin\gamma \ \ 0\,]_{\mathrm{F}_2}^{\top}$ pointing from G to F.

In terms of the tire-road interaction the contact patch is divided into an adhesion region of length λ and a sliding region of length $2a - \lambda$ (see Figure 5), where λ changes dynamically depending on the wheel's motion. When the shear force is below the maximum available static friction for a particular brush element, the brush element sticks to the road. Then the longitudinal and lateral sheer force components can be calculated by multiplying the longitudinal and lateral deformations of the brush elements with the longitudinal and lateral stiffnesses k_x and k_y and integrating along the adhesion region. In general, the deformations change dynamically along the adhesion region. However, as shown in Appendix B, assuming quasi-stationary wheel motion leads to linear increase of the deformation along the contact patch—as we move away from the leading point—both in the longitudinal and the lateral directions; see Figure 5.

As the deformation continues to increase along the contact patch, the required shear force eventually exceeds the maximum available static friction. In this case, the brush elements no longer stick to the road, and sliding occurs, as depicted at the rear part of the contact patch in Figure 5. Then the magnitude of the friction force for a brush element is equal to the sliding friction coefficient μ times the normal force pressing the brush element to the ground. In order to determine the longitudinal and lateral components of the friction force for each brush element sliding on the ground, one needs to obtain the sliding velocity of the brush element, as the force direction is opposite of this velocity. In general, for anisotropic tires (i.e., when the longitudinal stiffness and the lateral stiffness differ $k_x \neq k_y$) the direction of the sliding velocity varies along the sliding region. However, as shown in Appendix B, this variation is small and the sliding velocity can be well approximated by

$$\mathbf{v}_{\mathrm{s}} = \begin{bmatrix} -r\Omega + v_{\mathrm{O}} \cos\alpha \\ -v_{\mathrm{O}} \sin\alpha \\ 0 \end{bmatrix} = |r\Omega| \begin{bmatrix} -S_x \\ -S_y \\ 0 \end{bmatrix} , \tag{14}$$

along the whole sliding region. Thus, the direction of the friction force in the sliding region is given by the sliding angle β (see Figure 5), which can be defined as

$$\begin{aligned} \cos\beta &= -\frac{v_{\mathrm{s},x}}{v_{\mathrm{s}}} = \frac{S_x}{\sqrt{{S_x}^2 + {S_y}^2}} , \\ \sin\beta &= -\frac{v_{\mathrm{s},y}}{v_{\mathrm{s}}} = \frac{S_y}{\sqrt{{S_x}^2 + {S_y}^2}} , \\ \tan\beta &= \frac{v_{\mathrm{s},y}}{v_{\mathrm{s},x}} = \frac{S_y}{S_x} , \end{aligned} \tag{15}$$

where $v_{\mathrm{s}} = |\mathbf{v}_{\mathrm{s}}|$.

We remark that the assumption that the sliding velocity $\mathbf{v}_{\mathrm{s}}$, and in turn, the sliding angle β of the friction force is constant throughout the sliding region has been used in the literature [47], though strictly speaking it only holds for isotropic tires ($k_x = k_y$). This assumption barely influences the longitudinal and lateral forces but it makes the aligning moment somewhat unrealistic. As we are interested in the handling dynamics of the whole vehicle, the aligning moments have negligible effects. However, one may need to revisit the above assumption when studying steering dynamics, where the aligning moment plays an important role.

The adhesion length λ can be calculated based on when the magnitude of the sheer force reaches the limit given by the sticking friction (at the left end of the adhesion region). This yields

$$\lambda = 2a - \frac{4a^3}{3\mu_0 F_z} \sqrt{k_x^2 S_x^2 + k_y^2 S_y^2} , \tag{16}$$

where F_z is the resultant normal force acting on the contact patch. In the 5 DoF single track model, the normal forces $F_{z,\mathrm{f}}$ and $F_{z,\mathrm{r}}$ for the front and rear wheels can be calculated as

$$\begin{aligned} F_{z,\mathrm{f}} &= m_{\mathrm{w}} g + \frac{m_{\mathrm{v}} g d - M_{\mathrm{d}}}{l} , \\ F_{z,\mathrm{r}} &= m_{\mathrm{w}} g + \frac{m_{\mathrm{v}} g q + M_{\mathrm{d}}}{l} , \end{aligned} \tag{17}$$

respectively.

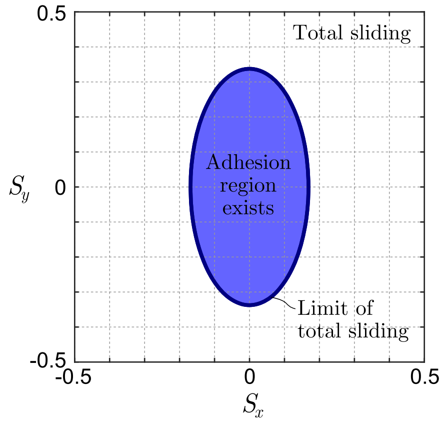

Figure 6. The adhesion ellipse (18) shaded blue when using the normal force $F_z = 5000\,\mathrm{N}$ and k_x, k_y, a, and μ_0 from Table 1

Note that the adhesion region only exists for $\lambda > 0$. Substituting this into (16) yields

$$k_x^2 S_x^2 + k_y^2 S_y^2 < \left(\frac{3\mu_0 F_z}{2a^2}\right)^2, \tag{18}$$

which corresponds to an ellipse in the (S_x, S_y)-plane; see Figure 6. In other words, if the longitudinal and lateral slips S_x and S_y are sufficiently large, sliding can occur for all brush elements and the adhesion region no longer exists. This is called total sliding or saturated tire, and occurs outside the elliptical region, that is, when

$$k_x^2 S_x^2 + k_y^2 S_y^2 \geq \left(\frac{3\mu_0 F_z}{2a^2}\right)^2. \tag{19}$$

We remark that for isotropic tires ($k_x = k_y$) the ellipse becomes a circle which is often referred to as the friction circle.

Based on the above results, the longitudinal tire force F_x, the lateral tire force F_y and the aligning moment M_z are given as functions of S_x and S_y:

$$\begin{aligned}
F_x(S_x, S_y) &= \begin{cases} \dfrac{\lambda^2}{2} k_x S_x + \dfrac{(2a-\lambda)^2(a+\lambda)}{4a^3}\mu F_z \cos\beta & \text{if } (18), \\ \mu F_z \cos\beta & \text{if } (19), \end{cases} \\
F_y(S_x, S_y) &= \begin{cases} \dfrac{\lambda^2}{2} k_y S_y + \dfrac{(2a-\lambda)^2(a+\lambda)}{4a^3}\mu F_z \sin\beta & \text{if } (18), \\ \mu F_z \sin\beta & \text{if } (19), \end{cases} \\
M_z(S_x, S_y) &= \begin{cases} \dfrac{(3a-2\lambda)\lambda^2}{6} k_y S_y - \dfrac{3(2a-\lambda)^2\lambda^2}{16a^3}\mu F_z \sin\beta & \text{if } (18), \\ 0 & \text{if } (19), \end{cases}
\end{aligned} \tag{20}$$

where β and λ should be substituted from (15) and (16), respectively. The detailed derivations can be found in Appendix B.

The friction forces and aligning moments are visualized by the surface plots in Figure 7 as functions of the longitudinal and lateral slips. The red curves in panels (a)-(b) highlight the pure longitudinal-slip case, while the red curves in panels (c)-(f)

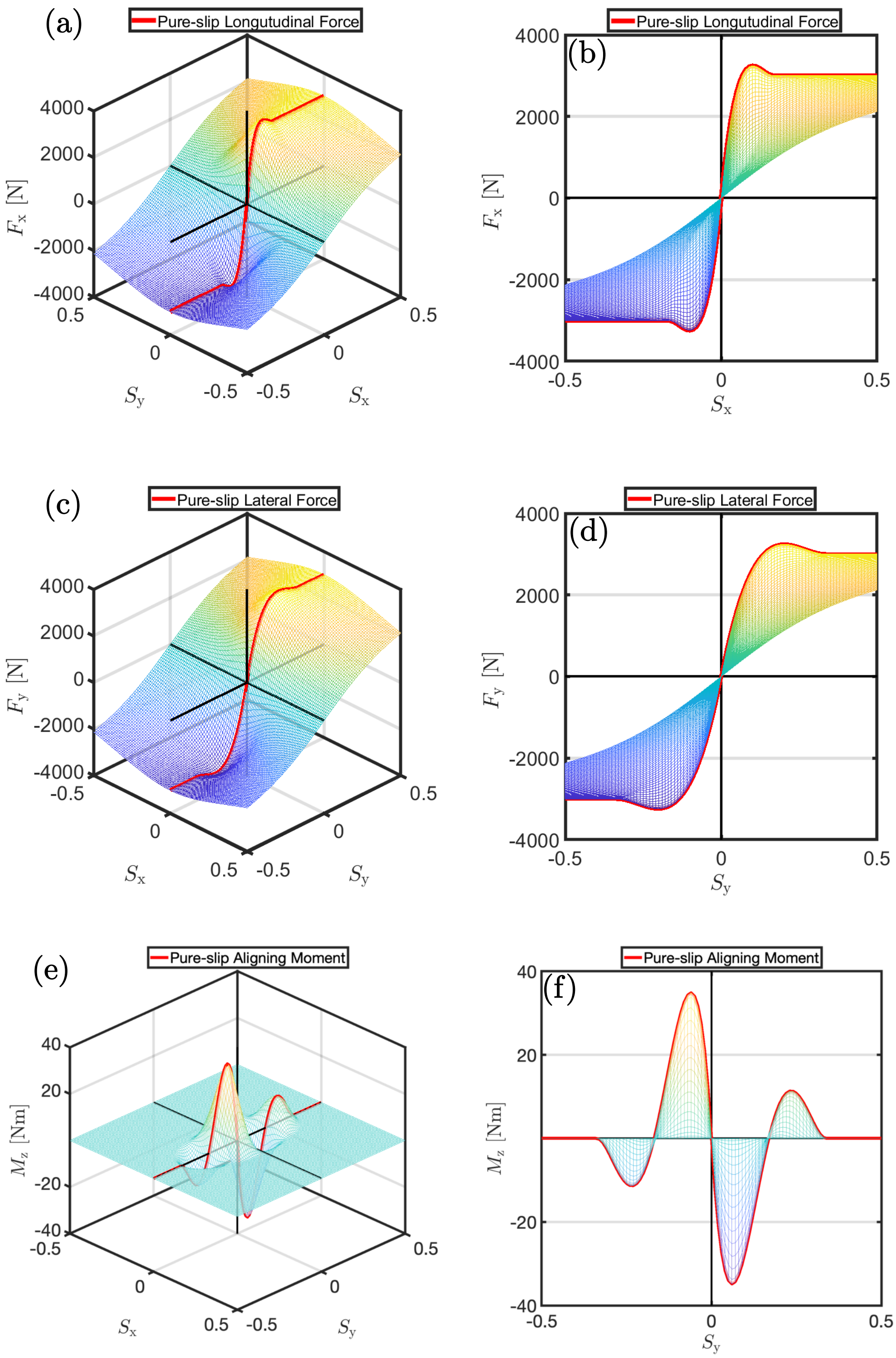

Figure 7. The longitudinal force F_x (a,b), the lateral force F_y (c,d), and the aligning moment M_z (e,f) as functions of the lateral slip S_x and longitudinal slip S_y for $F_z = 5000\,\mathrm{N}$ with the other parameters selected from Table 1

illustrate the pure lateral-slip case. The surfaces are indeed symmetric about these pure slip cases. Since the lateral stiffness k_y of the brush elements is smaller than the longitudinal stiffness k_x, total sliding first occurs at a larger S_y value in the pure lateral-slip case than the value of S_x in the pure longitudinal-slip case; cf. panels (b) and (d).

One may observe that the pure slip cases correspond to the largest tire-road friction. Therefore, when using a lower DoF vehicle model, where due to the lack of wheel speed dynamics the combined slip tire model cannot be incorporated, the available tire-road friction is overestimated. Prior Fiala model-inspired combined slip models such as [12,13,17] can capture the qualitative trends of the longitudinal and lateral force characteristics, but quantitative errors arise as these models do not differentiate the longitudinal and lateral stiffnesses. In addition, these models cannot describe the aligning moment depicted in panels (e)-(f) as captured by the new model.

3.3. Links between the 5 DoF and the traditional 2.5 DoF models

Before diving into the details of the analysis of 5 DoF model, we show how the equations of motion can be simplified to the traditional 2.5 DoF single track model presented in Section 2.

To obtain the traditional model the mass and the mass moment of inertia of the front and rear wheels have to be ignored:

$$m_{\mathrm{w}} = 0\,, \quad C = 0\,, \quad D = 0\,, \tag{21}$$

which yields $p = 0$ in (8). Then, the last two equations in (7) result in the longitudinal forces $F_{x,\mathrm{r}} = M_{\mathrm{d}}/r$ and $F_{x,\mathrm{f}} = 0$. Substituting these and the kinematic constraint $\dot{v} = 0$ into (7), the first equation can be used to obtain M_{d} while the second and third equations simplify to the first two equations in (1). Moreover, in (6) the last two equations can be ignored and the first three equations are identical to last three equations in (1).

In addition, the longitudinal slip S_x is zero, and thus, the first equation in (9) yields $r\Omega = v_{\mathrm{O}} \cos\alpha$. Substituting this into the second equation and exploiting $\Omega > 0$ yield $S_y = \tan\alpha$. Substituting $S_x = 0$ into (16) gives the adhesion length

$$\lambda = 2a - \frac{4k_y a^3}{3\mu_0 F_z}|S_y|\,, \tag{22}$$

while (18) simplifies to

$$|S_y| < S_{y,\mathrm{cr}} = \frac{3\mu_0 F_z}{2k_y a^2}. \tag{23}$$

Finally, since the tire friction force points the lateral direction in the sliding domain, we have

$$\begin{cases} \beta = \pi/2 & \text{if } \; S_y > 0, \\ \beta = 0 & \text{if } \; S_y = 0, \\ \beta = -\pi/2 & \text{if } \; S_y < 0, \end{cases} \tag{24}$$

which yields $\cos\beta = 0$ and $\sin\beta = \mathrm{sgn}(S_y)$, cf. (15). Consequently, the longitudinal tire force in (20) becomes zero while the lateral tire force and the aligning moment simplify to

$$
\begin{aligned}
F_y(S_y) &= \begin{cases} \dfrac{\lambda^2}{2} k_y S_y + \dfrac{(2a-\lambda)^2(a+\lambda)}{4a^3}\mu F_z \operatorname{sgn}(S_y), & \text{if } |S_y| < S_{y,\mathrm{cr}}, \\ \mu F_z \operatorname{sgn}(S_y), & \text{if } |S_y| \geq S_{y,\mathrm{cr}}, \end{cases} \\
M_z(S_y) &= \begin{cases} \dfrac{(3a-2\lambda)\lambda^2}{6} k_y S_y - \dfrac{3(2a-\lambda)^2\lambda^2}{16a^3}\mu F_z \operatorname{sgn}(S_y), & \text{if } |S_y| < S_{y,\mathrm{cr}}, \\ 0, & \text{if } |S_y| \geq S_{y,\mathrm{cr}}. \end{cases}
\end{aligned} \tag{25}
$$

Substituting (22) and $S_y = \tan\alpha$ results in (4)-(5).

4. Bifurcation Analysis of Steady States and Periodic Solutions

In this section we analyze the dynamics of the 5 DoF vehicle model introduced in Section 3.1. In particular, we focus on the essential dynamics (7) and investigate the steady states and periodic solutions while varying the control inputs, i.e., the steering angle γ and the driving torque M_d.

4.1. Steady States

We consider the steady state $v(t) \equiv v^*$, $\sigma(t) \equiv \sigma^*$, $\omega(t) \equiv \omega^*$, $\Omega_\mathrm{r}(t) \equiv \Omega_\mathrm{r}^*$, $\Omega_\mathrm{f}(t) \equiv \Omega_\mathrm{f}^*$ while subject to the steady state inputs $\gamma(t) \equiv \gamma^*$, $M_\mathrm{d}(t) \equiv M_\mathrm{d}^*$. Substituting these into (7) results in

$$
\begin{aligned}
0 &= m\sigma^*\omega^* + p\omega^{*2} + F_{x,\mathrm{r}}^* + F_{x,\mathrm{f}}^* \cos\gamma^* - F_{y,\mathrm{f}}^* \sin\gamma^*, \\
0 &= -(Jm - p^2)v^*\omega^* \\
&\quad + (J+pd)F_{y,\mathrm{r}}^* + (J-pq)(F_{y,\mathrm{f}}^* \cos\gamma^* + F_{x,\mathrm{f}}^* \sin\gamma^*) - p(M_{z,\mathrm{r}}^* + M_{z,\mathrm{f}}^*), \\
0 &= -(md+p)F_{y,\mathrm{r}}^* + (mq-p)(F_{y,\mathrm{f}}^* \cos\gamma^* + F_{x,\mathrm{f}}^* \sin\gamma^*) + m(M_{z,\mathrm{r}}^* + M_{z,\mathrm{f}}^*), \\
0 &= M_\mathrm{d}^* - rF_{x,\mathrm{r}}^*, \\
0 &= -rF_{x,\mathrm{f}}^*.
\end{aligned} \tag{26}
$$

Observe that the last two equations of (26) yield

$$
F_{x,\mathrm{r}}^* = \frac{M_\mathrm{d}^*}{r}, \quad F_{x,\mathrm{f}}^* = 0, \tag{27}
$$

that is, in steady state, the longitudinal force at the rear wheel is given by the applied driving torque while the longitudinal force at the front wheel is zero. According to (20), the latter also implies that the steady state longitudinal slip at the front wheel is zero: $S_{x,\mathrm{f}}^* = 0$; see also Figure 7(c). Substituting (27) in the first three equations of (26) yields

$$
\begin{aligned}
0 &= m\sigma^*\omega^* + p\omega^{*2} + \frac{M_\mathrm{d}^*}{r} - F_{y,\mathrm{f}}^* \sin\gamma^*, \\
0 &= -(Jm - p^2)v^*\omega^* + (J+pd)F_{y,\mathrm{r}}^* + (J-pq)F_{y,\mathrm{f}}^* \cos\gamma^* - p(M_{z,\mathrm{r}}^* + M_{z,\mathrm{f}}^*), \\
0 &= -(md+p)F_{y,\mathrm{r}}^* + (mq-p)F_{y,\mathrm{f}}^* \cos\gamma^* + m(M_{z,\mathrm{r}}^* + M_{z,\mathrm{f}}^*).
\end{aligned} \tag{28}
$$

Table 2. Different types of steady state solutions

$\gamma^* = 5°$	v^* $[\frac{\text{m}}{\text{s}}]$	σ^* $[\frac{\text{m}}{\text{s}}]$	ω^* $[\frac{\text{rad}}{\text{s}}]$	Ω^*_{r} $[\frac{\text{rad}}{\text{s}}]$	Ω^*_{f} $[\frac{\text{rad}}{\text{s}}]$	$S^*_{x,\text{r}}$	$S^*_{y,\text{r}}$	$S^*_{x,\text{f}}$	$S^*_{y,\text{f}}$	M^*_{d} [Nm]
S. S. Cornering	14.96	−0.84	0.29	50.56	49.75	0.01	0.09	0	0.13	200
Donut	5.52	−1.31	0.91	24.79	18.22	0.26	0.36	0	0.16	622
Drifting	13.63	4.02	−0.39	54.64	46.33	0.17	−0.28	0	−0.18	545

The steady state lateral tire forces $F^*_{y,\text{r}}, F^*_{y,\text{f}}$ and the aligning moments $M^*_{z,\text{r}}, M^*_{z,\text{f}}$ are functions of the steady states according to the slip definitions (11), (13) and the combined slip tire model (15), (16), (20). Thus, given the steering angle γ^* and the driving torque M^*_{d}, one may solve (27), (28) for the steady states v^*, σ^*, ω^*, Ω^*_{r}, Ω^*_{f}.

Before discussing the general solutions we highlight the special case of the rectilinear motion. Notice that substituting $\gamma^* = 0$, $M^*_{\text{d}} = 0$, $\sigma^* = 0$, $\omega^* = 0$ into (28), the first equation is satisfied. Moreover, according to (11), (13), the lateral slips are zeros $S^*_{y,\text{r}} = 0$, $S^*_{y,\text{f}} = 0$, which result in zero lateral forces $F^*_{y,\text{r}} = 0$, $F^*_{y,\text{f}} = 0$ and zero aligning moments $M^*_{z,\text{r}} = 0$, $M^*_{z,\text{f}} = 0$. Thus, the last two equation in (28) are satisfied for arbitrary longitudinal speed v^*. Finally, according to (11), (13), the wheel speeds are $\Omega^*_{\text{r}} = v^*/r$, $\Omega^*_{\text{f}} = v^*/r$. In summary, when no steering and driving torque inputs are applied, the rectilinear solution exists for any constant speed.

When applying nonzero constant inputs $\gamma^* \neq 0$, $M^*_{\text{d}} \neq 0$ the algebraic equations (11), (13), (15), (16), (20), (27), (28) need to be solved for v^*, σ^*, ω^*, Ω^*_{r}, Ω^*_{f}, numerically. We utilize the multi-dimensional bisection method (MDBM) [46], which can return all solutions in user-defined domains in the state space without requiring an initial guess. One may find three qualitatively different solutions: steady state cornering, donut, and drifting, as presented for $\gamma^* = 5°$ in Table 2. Steady state cornering represents the scenario where the vehicle is turning with relatively low lateral velocity and yaw rate while both the rear tire and the front tire are well below their saturation limits:

$$k_x^2 S^{*2}_{x,\text{r}} + k_y^2 S^{*2}_{y,\text{r}} \ll \left(\frac{3\mu_0 F_{z,\text{r}}}{2a^2}\right)^2, \qquad k_x^2 S^{*2}_{x,\text{f}} + k_y^2 S^{*2}_{y,\text{f}} \ll \left(\frac{3\mu_0 F_{z,\text{f}}}{2a^2}\right)^2. \tag{29}$$

cf. (18), (19). Donut refers to a state when the vehicle is turning with large lateral velocity and yaw rate while the rear tire is saturated and the front tire is still below the saturation limit:

$$k_x^2 S^{*2}_{x,\text{r}} + k_y^2 S^{*2}_{y,\text{r}} > \left(\frac{3\mu_0 F_{z,\text{r}}}{2a^2}\right)^2, \qquad k_x^2 S^{*2}_{x,\text{f}} + k_y^2 S^{*2}_{y,\text{f}} < \left(\frac{3\mu_0 F_{z,\text{f}}}{2a^2}\right)^2. \tag{30}$$

When drifting, the vehicle is also turning with large lateral velocity and yaw rate while the rear tire is saturated and the front tire is below the saturation limit, i.e., (30) still holds. However, compared to the donut, the vehicle is turning in the opposite direction of the steering input.

In summary, the vehicle can exhibit three types of steady state motions for a constant steering angle. For small driving torque, the vehicle corners slowly with small tire slips. For large driving torque, two motions with rapid turning and large tire slips are possible: donut and drifting. When drawing donuts the vehicle turns to the same direction as the steering input, while when drifting it turns the opposite direction.

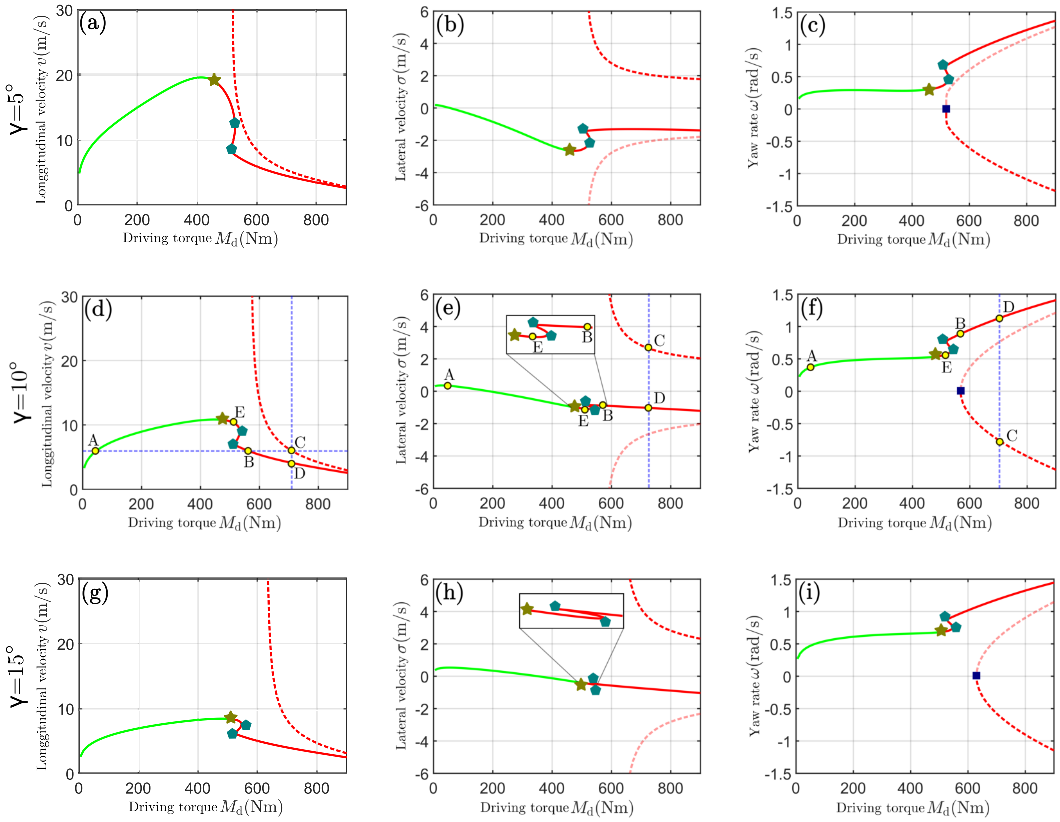

Figure 8. Bifurcation diagrams for the longitudinal velocity, lateral velocity and yaw rate with driving torque as the bifurcation parameter. Green and red branches correspond to stable and unstable steady states, respectively. Teal pentagons mark the fold bifurcation points, olive stars mark Hopf bifurcation points, and navy blue squares correspond to singularities.

4.2. Bifurcation Analysis of Steady States

In this subsection, we analyze the steady states of the 5 DoF model (7) when varying the control inputs. We plot the results using bifurcation diagrams which indicate the stability of steady states: green color is used for stable states and red color is used for unstable ones. This color code will be kept for the rest of the paper. The transitions (bifurcation points) between stable and unstable states are marked by different symbols as explained further below. The bifurcation diagrams are generated by the numerical continuation software package DDE-Biftool [43,44]. The different steady states discovered through this bifurcation analysis will be utilized to design and control different maneuvers in Section 5.

Figure 8 shows the steady state values of the longitudinal velocity v, the lateral velocity σ, and the yaw rate ω, while varying the constant driving torque M_d. Each row corresponds to a constant steering angle γ, as indicated. The three rows show qualitatively similar dynamics but one may observe quantitative differences as will be discussed further below. For each value of γ two branches of steady states are obtained: the solid one changes stability as the torque is increased while the dashed one is always unstable—though it only exists above a certain torque value.

For lower torque values the solid branch is stable (green section) and this corresponds to the steady state cornering, i.e., the vehicle is turning with small yaw rate ω.

As M_d is increased, the steady state loses stability through a Hopf bifurcation (olive star), which is followed by two fold bifurcations (teal pentagons). Notice that the Hopf point is located in the vicinity of the maximum longitudinal speed, that is, the vehicle is close to its handling limit. Increasing the driving torque further, the longitudinal velocity drops sharply while yaw rate increases significantly as going through the fold points. After passing the second fold point, the system enters the donut regime.

As the steady state loses stability at the Hopf point, a pair of complex conjugate characteristic roots move to the right half of the complex plane. The unstable pair of complex conjugate eigenvalues becomes real between the Hopf point and the first fold point. One of these real eigenvalues moves to the left half complex plane at first the fold point and moves back to the right half complex plane at the second fold point. The unstable eigenvalues become complex conjugate again in the vicinity of the second fold point. The two fold bifurcations neither influence the stability of the steady state, nor change the limit cycle oscillations arising from the Hopf bifurcation; the latter are examined in detail in Section 4.3. One may show, however, that in the special case of $\mu = \mu_0$ (not presented in the figures) the fold bifurcations disappear and the longitudinal velocity decreases faster as the driving torque is increased. This emphasizes the importance of differentiating the friction coefficients in the model.

Aside from the steady state cornering/donut branch (solid green/red), drifting branches (dashed red) are also detected for sufficiently large driving torque. The larger the steering angle is the larger torque is needed for drifting to appear. For completeness, we also include the drifting branches for the negative steering inputs $\gamma = -5°$, $\gamma = -10°$, $\gamma = -15°$; these are differentiated by the lighter red color in panels (b), (c), (e), (f), (h), (i). Due to symmetry, the drifting branches for positive and negative steering inputs coincide in their longitudinal velocity; see panels (a), (d), (g). The drifting branches have vertical asymptotes in panels (a), (b), (d), (e), (g), (h), but they arose from the singular points (navy blue squares) in panels (c), (f), (i).

Observe that the singular point of the drifting branch is on the right of the Hopf point of the steady state cornering/donut branch. This implies that the drifting motion cannot be initiated for torque values that result in stable steady state cornering. Moreover, the drifting solutions of negative steering inputs and the donut solution of positive steering are close to each other. This could explain why drivers often initiate a drifting maneuver by first performing a donut and then suddenly applying counter steering, as it will also be demonstrated in Section 5.

Last but not least, we discuss the effects of the steering input γ by comparing the three rows in Figure 8. Comparing panels (a), (d) and (g), we can see that as γ increases, the longitudinal velocity of the vehicle decreases significantly for steady state cornering and donut. It is because the lateral tire force at the front wheel has a larger resistance in the longitudinal direction of the vehicle. This also explains why the drifting requires larger driving torque input as the steering input increases, while the speed remains similar. In other words, the drifting branch shifts to right as the steering angle is increased.

In conclusion, for a given constant steering input γ, we have three driving torque regimes. If the driving torque is smaller than that of the Hopf point, there exist a stable steady state cornering solution. If the driving torque is in between the Hopf point and the singular point, the steady state becomes unstable and only donut is possible. If the driving torque is above the singular point, donut and drifting steady states coexist, though they are both unstable (without feedback control). Finally, when considering a constant longitudinal speed the three steady states may coexist as illustrated by the points A, B, C marked in Figure 8. While this was already predicted by the traditional 2.5 DoF model (cf. Figure 3), that simplified model failed to capture the different driving torques needed to maintain these steady states. More details about the steady states corresponding to the points A, B, C, D, E marked in Figure 8 are provided in the next subsection together with the analysis of periodic solutions.

4.3. Bifurcation Analysis of Periodic Solutions

Here we take a closer look at the limit cycle oscillations arising from the Hopf bifurcations. We compare these solutions to the steady states using phase portraits, i.e., trajectories in state space, and by observing the motion of the center of mass in physical space. This provides us with insight about what happens when the vehicle is driving in a steady state or along a periodic solution, and also provides us with information about the local dynamics around these invariant solutions.

The results related to the Hopf bifurcation are shown in Figure 9. In panel (a), we trace the Hopf bifurcation boundary in the (M_{d}, γ) plane. The gold curve show the stability boundary: the steady state cornering/donut is stable above and unstable below this curve as indicated by green and red shading. In order to investigate the periodic oscillations arising from the Hopf bifurcation we investigate the system along the horizontal dashed line segments at $\gamma = 5°$ between $M_{\mathrm{d}} \in [460, 530]$ Nm, at $\gamma = 10°$ between $M_{\mathrm{d}} \in [480, 550]$ Nm, and at $\gamma = 15°$ between $M_{\mathrm{d}} \in [500, 550]$ Nm. The arising branches of periodic solutions are depicted in panels (b), (d) and (f) for the three different steering inputs through the amplitude of the longitudinal velocity v as a function of the driving torque. Panels (c), (e) and (g) show the same branches in zoomed domains close to the Hopf bifurcation.

For smaller steering angles ($\gamma = 5°$ and $\gamma = 10°$) the Hopf bifurcation is supercritical, that is, a branch of stable periodic oscillations arises. As the torque is increased, this solution loses stability via a period doubling bifurcation (light blue diamond) and then gains stability again via nonsmooth bifurcation (vertical gray dashed line) through which the amplitude of the oscillations also increases significantly. For larger steering angles ($\gamma = 15°$) the Hopf bifurcation is subcritical, that is, a branch of stable oscillations arises, which again gains stability and increases its amplitude through a nonsmooth bifurcation. One may observe that in all cases the amplitude does not change significantly when increasing the torque input beyond the nonsmooth bifurcation. On the other hand, the amplitude decreases when increasing the steering angle input. While the detailed analyses of the Hopf bifurcation and the nonsmooth bifurcation are left for future research, we study the arising periodic orbits in detail.

For the case $\gamma = 10°$, we labeled the steady states A, B, C, D, E in Figure 8 and the periodic solutions H, G in Figure 9. The corresponding torque values are $M_{\mathrm{d}} = 54.1$ Nm for case A, $M_{\mathrm{d}} = 541.5$ Nm for cases B and H, $M_{\mathrm{d}} = 696.7$ Nm for cases C and D, and $M_{\mathrm{d}} = 487.7$ Nm for cases E and G. We display the corresponding phase portraits in the plane of the side slip angle $\arctan(\sigma/v)$ and yaw rate ω in Figure (10). The steady states (colored dots) and the periodic orbits (colored curves) are extracted from the continuation software DDE-Biftool, while the black trajectories are obtained via numerical simulations from different initial conditions. Note that the trajectories may intersect each other since we are projecting them from the 5-dimensional state space of (7) onto the 2-dimensional plane. To have more physical insights on different types of steady states and periodic orbits, we plot the trace of the center of mass G in the (x, y) plane in Figure 11. This is obtained by solving the kinematic equations (6) for the numerical continuation results such that the vehicle stars from the origin

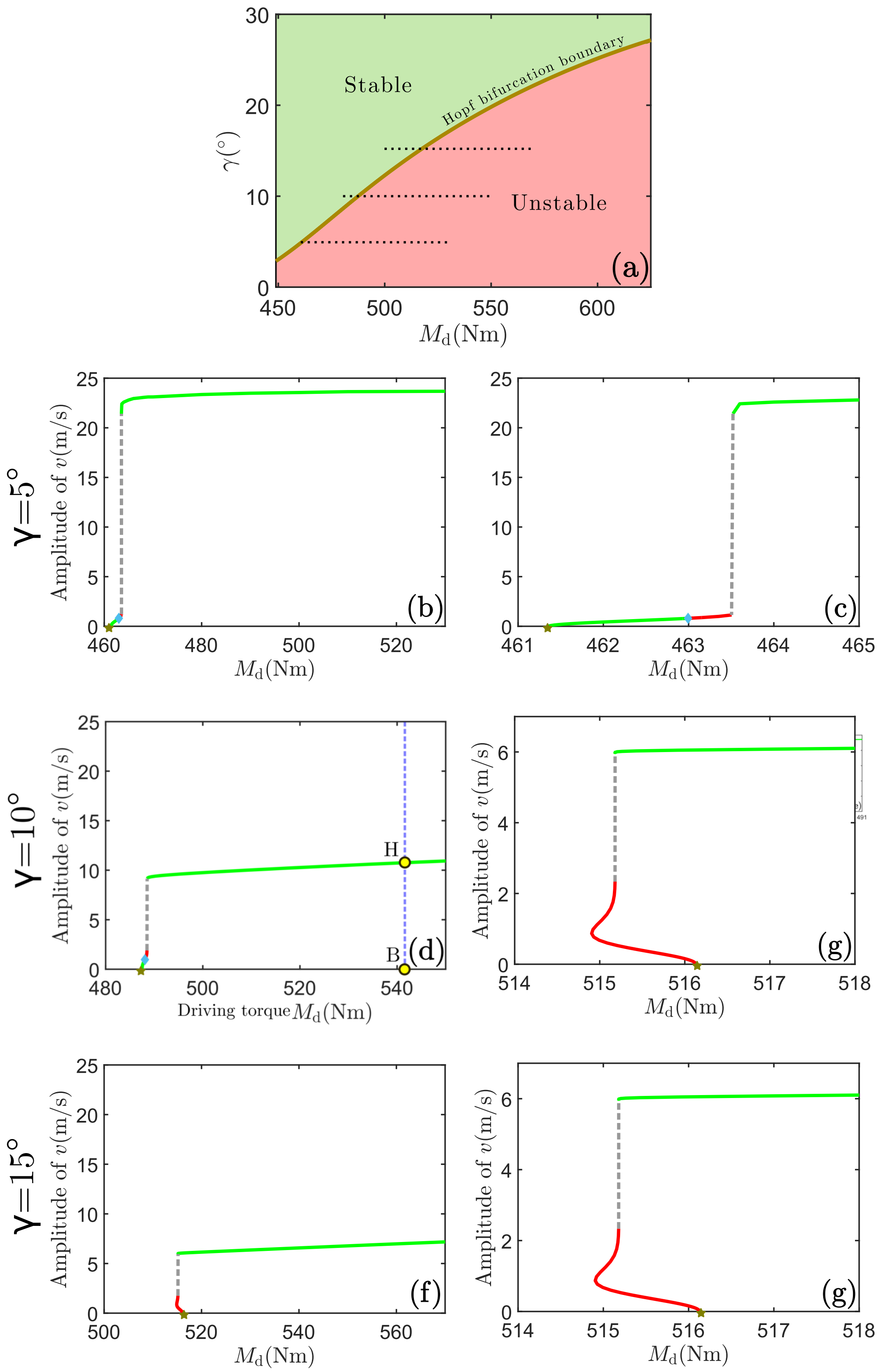

Figure 9. (a) Stability diagram for the steady state cornering/donut steady state on the plane of driving torque and steering angle. (b),(d),(f) Bifurcation diagrams for the longitudinal velocity with driving torque as the bifurcation parameter. (c),(e),(g) zoomed versions of the bifurcation diagrams.

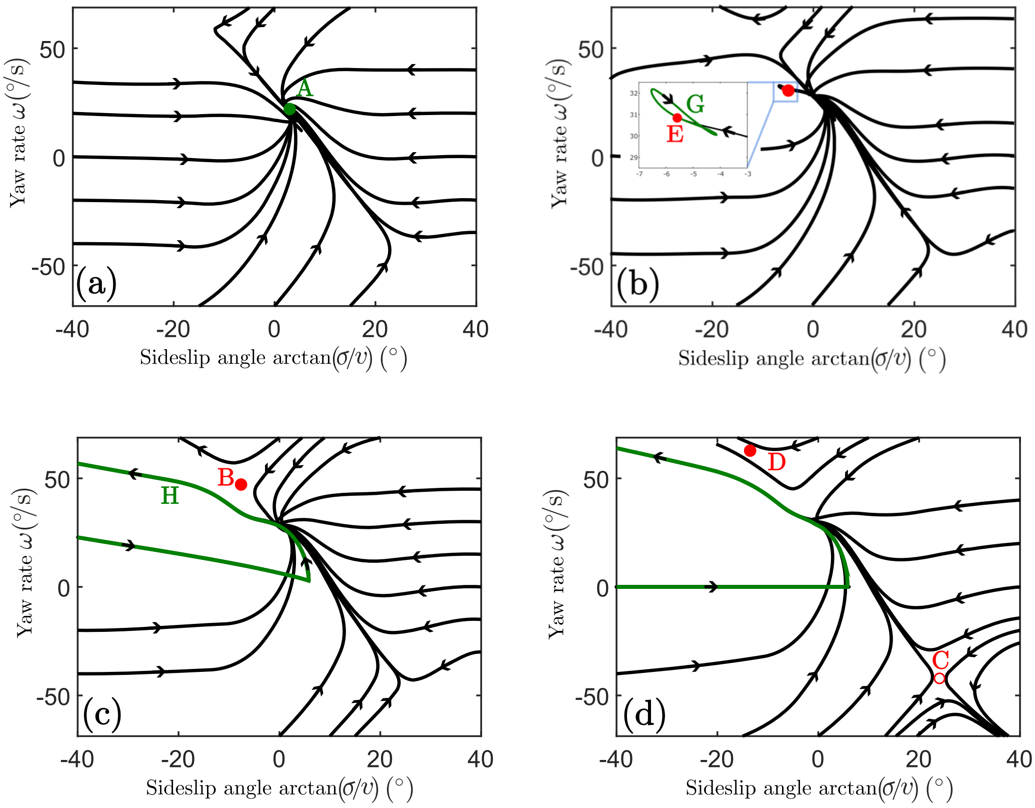

Figure 10. Phase portraits in the plane of the side slip angle and yaw rate for the solutions marked in Figures 8 and 9 for $\gamma = 10°$. The corresponding torque values are (a) $M_\mathrm{d} = 54.1\,\mathrm{Nm}$, (b) $M_\mathrm{d} = 487.7\,\mathrm{Nm}$, (c) $M_\mathrm{d} = 541.5\,\mathrm{Nm}$, and (d) $M_\mathrm{d} = 696.7\,\mathrm{Nm}$.

for all trajectories. Green and red colors are still used to differentiate trajectories corresponding to stable and unstable states.

Considering the steady state cornering solution A (marked for $\gamma = 10°$, $M_\mathrm{d} = 54.1\,\mathrm{Nm}$ in Figure 8), this state is globally asymptotically stable. Correspondingly, all trajectories converge to this state in Figure 10(a). In this steady state the vehicle is driving on the circular trajectory in the counterclockwise direction with constant speed as shown in Figure 11(a).

As the driving torque input is increased to $M_\mathrm{d} = 487.7\,\mathrm{Nm}$, the steady state cornering solution E in Figure 8 becomes unstable and the small amplitude (globally) stable periodic solution G appears as shown in Figure 9(e). These orbits are highlighted Figure 10(b) using a zoomed inlet. In Figure 11(b), the corresponding traces of the center of mass G in are shown by the red circle and the green quasiperiodic motion, respectively. To further illustrate the periodic solution, we plot the time profiles of the state variables v, σ, and ω together with the longitudinal slips $S_{x,\mathrm{r}}$, $S_{x,\mathrm{f}}$ and lateral slips $S_{y,\mathrm{r}}$, $S_{y,\mathrm{f}}$ in Figure 12. As highlighted in panel (f), both the front and rear tires are within their saturation limits: both S_x and S_y remain inside their ellipse of total sliding. That is, even though the steady state is unstable, when driving along the periodic solution the vehicle still remains within its handling limits. In fact, the trajectory resembles the“out-in-out” cornering strategy used by professional race car drivers as they are fully exploiting the handling limits in order to minimize the curvature of the trajectory and maximize the exiting speed. However, as shown in Figure 9(d),(e), the

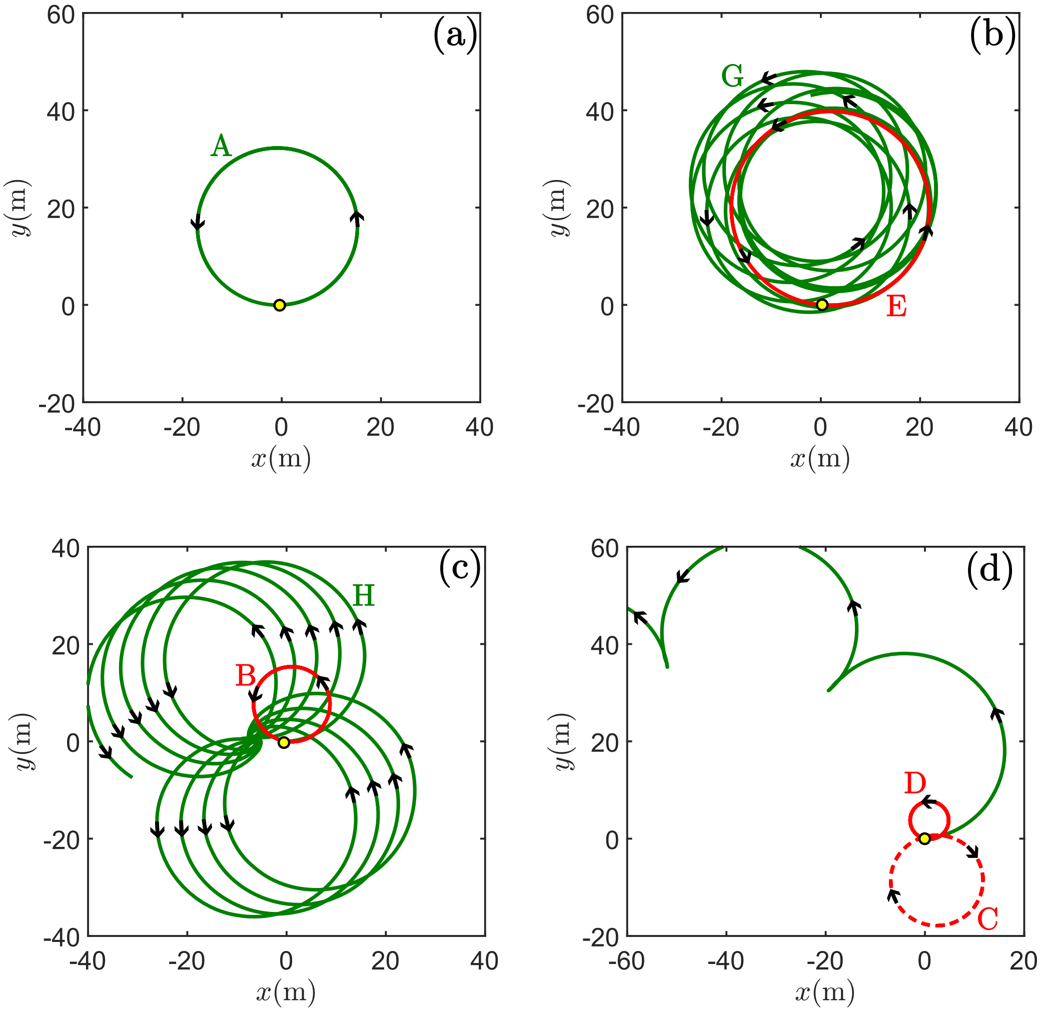

Figure 11. Trajectories of the center of gravity G of the vehicle for the solutions marked in Figures 8 and 9 for $\gamma = 10°$. The corresponding torque values are (a) $M_\mathrm{d} = 54.1\,\mathrm{Nm}$, (b) $M_\mathrm{d} = 487.7\,\mathrm{Nm}$, (c) $M_\mathrm{d} = 541.5\,\mathrm{Nm}$, and (d) $M_\mathrm{d} = 696.7\,\mathrm{Nm}$.

small amplitude periodic solutions only exist in a narrow band of driving torque in the vicinity of the Hopf birfurcation, and increasing the torque further results in large amplitude oscillations.

When increasing the driving torque to $M_\mathrm{d} = 541.5\,\mathrm{Nm}$, we obtain the (unstable) steady state cornering solution B in Figure 8 and the large amplitude stable periodic solution H appears in Figure 9(d). These orbits are highlighted Figure 10(c) where the large amplitude limit cycle is only partially visible in the window. The corresponding traces of the center of mass G are shown in Figure 11(c). The time profiles of the state variables and the longitudinal and lateral slips are plotted in Figure 13. Within one period of oscillation, the vehicle first corners with an increasing longitudinal velocity and decreasing lateral velocity, resulting a path with large radius of curvature. However, as the longitudinal velocity reaches its maximum value, the vehicle is no longer able to recover the tire traction and a sudden change of the tire slip occurs. In this process, the vehicle essentially spins out, as indicated by large values of lateral velocity and yaw rate, and eventually comes to a full stop after turning almost 180° at a very

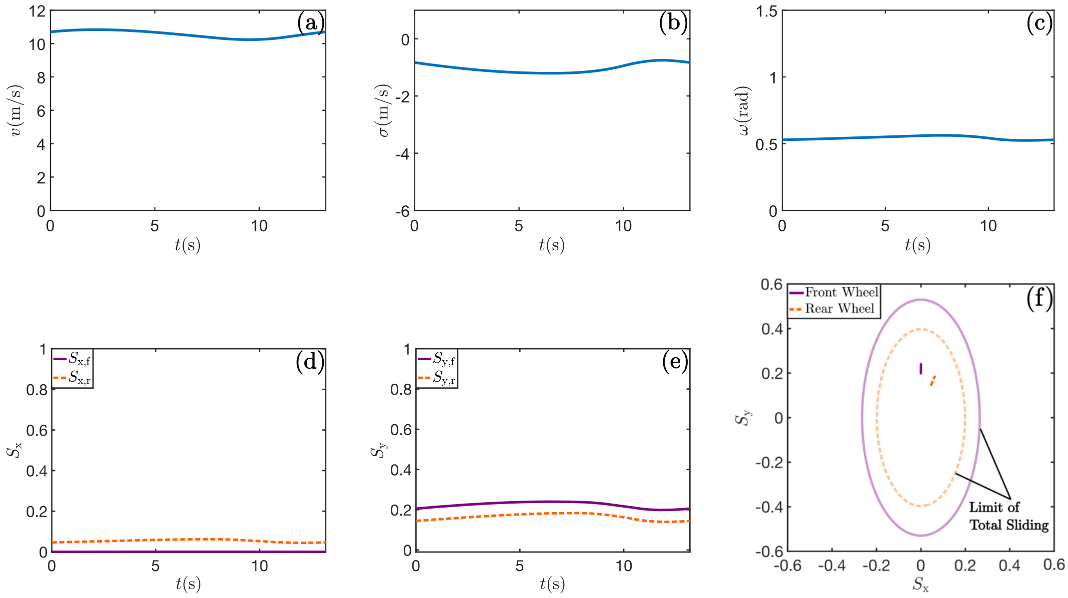

Figure 12. Times profiles for the state variables and the slips for the periodic solution at point G in Figures 9(e), 10(b) and 11(b).

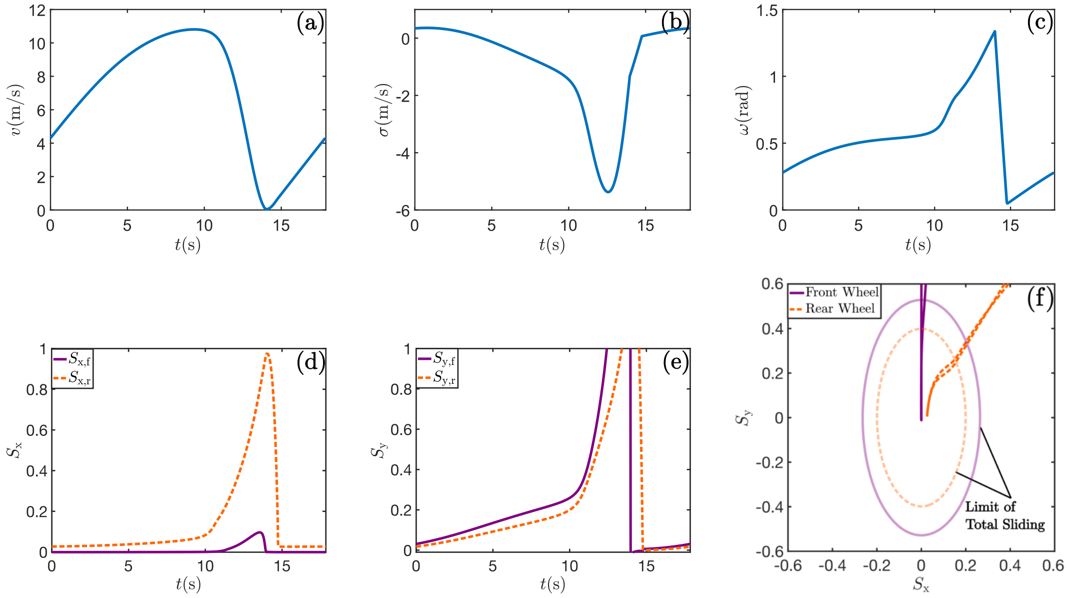

Figure 13. Times profiles for the state variables and the slips for the periodic solution at point H in Figures 9(d), 10(c) and 11(c).

small time period. Then, as the tire traction is recovered, the motion is repeated again. Figure 13(f) highlights that both the front and rear tires exceed their saturation limits while driving along the periodic orbit. The observed motion correspond to a handling scenario in which the vehicle is only able to recover the tire traction by coming to a full stop while spinning out.

Last but not least, we investigate the drifting solutions that appear for sufficiently large driving torques. Namely, setting the driving torque to $M_{\mathrm{d}} = 696.7\,\mathrm{Nm}$ we obtain two unstable steady states: the drifting C and the donut D as shown in Figure 8, and a large amplitude stable periodic solution also appears, which is out window in Figure 9(d). These orbits are plotted Figure 10(d) where the donut and drifting are differentiated by the red dot and red circle, cf. Figure 3(c). The corresponding traces of the center of mass G are shown in Figure 11(d) where the donut and drifting are shown by the solid and dashed circles, cf. Figure 3(d). Indeed, the donut is in the counterclockwise while the drifting is in the clockwise direction. Since both steady state solutions are unstable, the vehicle trajectory eventually converges to the large amplitude (globally) stable periodic orbit (solid green curve), which is similar to that in Figures 10(c) and 11(c). However, by applying feedback control, one may stabilize these unstable steady states as will be discussed in the next section.

5. Controlling Extreme Maneuvers

The nonlinear analysis of the 5 DoF model showed that the donut and drifting solutions generally have much larger lateral velocity and yaw rate than the steady state cornering solutions belonging to the same longitudinal velocity, cf. point A, B, C in Figure 8. Consequently, the vehicle traces a circle with smaller radius of curvature, see Figure 11. Hence, these solutions provide more maneuverability for extreme conditions, such as an evasive maneuver while avoiding a collision. The donut and the drifting solution have their own advantages compared to each other when negotiating tight corners. The donut has larger yaw rate that leads to smaller radius of curvature, while the drifting has larger lateral velocity, especially for smaller driving torque inputs. However, without feedback control both the donut and the drifting are unstable. Therefore, in this section, building on the results of the nonlinear analysis, we design feedback controllers to stabilize the unstable steady states. More importantly, we also demonstrate that by switching the controllers, it is also possible to transition the vehicle between different solutions. This flexibility enables automated vehicle to perform a variety of extreme handling maneuvers.

Assume that we would like to stabilize the unstable steady state

$$\mathbf{x}^* = \begin{bmatrix} v^* & \sigma^* & \omega^* & \Omega_\mathrm{r}^* & \Omega_\mathrm{f}^* \end{bmatrix}^\top , \tag{31}$$

obtained for the steady state input

$$\mathbf{u}^* = \begin{bmatrix} \gamma^* & M_\mathrm{d}^* \end{bmatrix}^\top , \tag{32}$$

which can be chosen according to the numerical continuation results. Then, we can define the state and input perturbation as

$$\tilde{\mathbf{x}} = \mathbf{x} - \mathbf{x}^* = \begin{bmatrix} v \\ \sigma \\ \omega \\ \Omega_\mathrm{r} \\ \Omega_\mathrm{f} \end{bmatrix} - \begin{bmatrix} v^* \\ \sigma^* \\ \omega^* \\ \Omega_\mathrm{r}^* \\ \Omega_\mathrm{f}^* \end{bmatrix} , \tag{33}$$

and

$$\tilde{\mathbf{u}} = \mathbf{u} - \mathbf{u}^* = \begin{bmatrix} \gamma \\ M_\mathrm{d} \end{bmatrix} - \begin{bmatrix} \gamma^* \\ M_\mathrm{d}^* \end{bmatrix}. \tag{34}$$

Then the essential dynamics (7) can be linearized around the unstable steady state yielding the linear system

$$\dot{\tilde{\mathbf{x}}} = \mathbf{A}\tilde{\mathbf{x}} + \mathbf{B}\tilde{\mathbf{u}}, \tag{35}$$

where the state matrix $\mathbf{A}$ and input matrix $\mathbf{B}$ can be computed as the Jacobian matrices with respect to the state vector $\mathbf{x}$ and input vector $\mathbf{u}$. Note that since the tire characteristics (20) are piece-wise smooth functions, the matrices $\mathbf{A}$ and $\mathbf{B}$ can be determined considering the longitudinal and lateral slip values related to the chosen steady state. If the controllability matrix of the pair $(\mathbf{A}, \mathbf{B})$ is full rank, the linearized system is controllable, and in turn, stabilizable. One may check numerically that this is indeed the case for the unstable steady states we consider.

Once an equilibrium and its stabilizability are known, one may use a plethora of different control techniques to stabilize it. For simplicity and computational efficiency, here we utilize the infinite-horizon linear quadratic regulator (LQR) that results in a state feedback controller. Namely, the LQR problem is formulated as

$$\begin{aligned} \min_{\tilde{\mathbf{u}}:[0,\infty]\to\mathbb{R}^2} & \int_0^\infty (\tilde{\mathbf{x}}^\mathrm{T}\mathbf{Q}\tilde{\mathbf{x}} + \tilde{\mathbf{u}}^\mathrm{T}\mathbf{R}\tilde{\mathbf{u}})\,\mathrm{d}t, \\ \text{subject to} \quad & \dot{\tilde{\mathbf{x}}} = \mathbf{A}\tilde{\mathbf{x}} + \mathbf{B}\tilde{\mathbf{u}}, \end{aligned} \tag{36}$$

where $\mathbf{Q}$ is the state penalty matrix and $\mathbf{R}$ is the input penalty matrix. For the sake of simplicity, these are set to

$$\mathbf{Q} = \begin{bmatrix} 1 & 0 & 0 & 0 & 0 \\ 0 & 1 & 0 & 0 & 0 \\ 0 & 0 & 1 & 0 & 0 \\ 0 & 0 & 0 & 1 & 0 \\ 0 & 0 & 0 & 0 & 1 \end{bmatrix}, \qquad \mathbf{R} = \begin{bmatrix} 1/2 & 0 \\ 0 & 1/2 \end{bmatrix}, \tag{37}$$

with the appropriate SI units considered.

The optimization problem (36) can be solved analytically, yielding the feedback law

$$\tilde{\mathbf{u}} = \mathbf{K}\tilde{\mathbf{x}}, \tag{38}$$

where the proportional gain matrix $\mathbf{K}$ can be obtained as

$$\mathbf{K} = -\mathbf{R}^{-1}\mathbf{B}^\mathrm{T}\mathbf{P}, \tag{39}$$

and the matrix $\mathbf{P}$ is the solution to the algebraic Riccati equation

$$\mathbf{A}^\mathrm{T}\mathbf{P} + \mathbf{P}\mathbf{A} - \mathbf{P}\mathbf{B}\mathbf{R}^{-1}\mathbf{B}^\mathrm{T}\mathbf{P} + \mathbf{Q} = \mathbf{0}. \tag{40}$$

In case of the drifting state C and donut state D found in Section 4.3 for

$\gamma = 10°, M_\mathrm{d} = 696.7\,\mathrm{Nm}$ we obtain the gain parameters

$$\begin{aligned}\mathbf{K}_\mathrm{C} &= \begin{bmatrix} -3.2418 & 2.0429 & -7.9585 & -0.0197 & -1.1311 \\ -0.2272 & -0.1002 & 0.2201 & -0.0315 & -0.0023 \end{bmatrix}, \\ \mathbf{K}_\mathrm{D} &= \begin{bmatrix} 2.1612 & 5.2897 & -13.0428 & 0.1002 & 0.9900 \\ -0.2204 & 0.0926 & -0.3553 & -0.0235 & -0.0023 \end{bmatrix}.\end{aligned} \tag{41}$$

In summary, the input of the stabilizing LQR controller is given by

$$\mathbf{u} = \mathbf{u}^* + \tilde{\mathbf{u}} = \mathbf{u}^* + \mathbf{K}(\mathbf{x} - \mathbf{x}^*). \tag{42}$$

In order to make the controller more practical and reflect the capabilities of consumer vehicles, we saturate the steering input (42) at $-30°$ and $30°$ and limit the driving torque input in the range of 0 Nm and 900 Nm.

We validate the performance of the LQR controller using numerical simulations. First, we demonstrate the stabilization of the drifting steady state C and the donut steady state D while using the gain matrices $\mathbf{K}_\mathrm{C}$ and $\mathbf{K}_\mathrm{D}$, respectively, see (41). Then we demonstrate that one may transition the vehicle between these two steady states by switching the controllers.

Figure 14 shows the simulation results where we either engage the counterclockwise donut controller (cyan curves) or the clockwise drifting controller (dark blue curves), such that the vehicle starts from standstill from the origin. The trace of the center of mass G on the (x, y) plane is plotted in panel (a), the vehicle states are shown in panels (b)-(d), and the control inputs are depicted in panels (e)-(f). Observe that the donut controller and the drifting controller, designed using the linearized systems, enable the vehicle to converge to the respective steady states with no steady state error. However, panels (c) and (d) show that, the drifting controller executes a maneuver by initially putting the vehicle in a transient counterclockwise donut motion before converging to the clockwise drifting steady state. During the time period between 4 s and 6 s, the controller executes two rapid steering maneuvers and then converges to the steady state input (which is very close to that of the counterclockwise donut). This simulation demonstrates the value of combining the bifurcation analysis (which determines the different steady states) with simple, computationally efficient control design (that stabilizes the steady states). It also corroborates the conclusion, revealed by the bifurcation analysis, that the drifting motion cannot be directly initiated from standstill because of the singularity point shown in Figure 8.

Now we demonstrate the capability of our control framework to converge to drifting via counter steering from a donut motion, a technique which is often used by professional race car drivers. Figure 15 shows the corresponding simulation results. We initially engage the counterclockwise donut controller to reach the donut solution D, when starting from standstill from the origin. Then at time 40 s, we switch to the counterclockwise drifting controller aiming for the drifting solution with a steady state input of $(\gamma = -10°, M_\mathrm{d} = 696.7\,\mathrm{Nm})$. Notice that this drifting steady state is the counterpart of point C with the exact opposite steady-state steering input, cf. Figures 14 and 15. Consequently, the steady state longitudinal velocity are the same while the steady state lateral velocity and yaw rate are the opposite of those of in C. And, indeed, the steady state trajectory is a circle with the same radius as that of C but the direction being counterclockwise. As illustrated by the states in panels (b)–(d), the vehicle is able to converge to the drifting steady state from the stabilized donut. In panel (e), a rapid counter steering input is observed when the drifting controller is

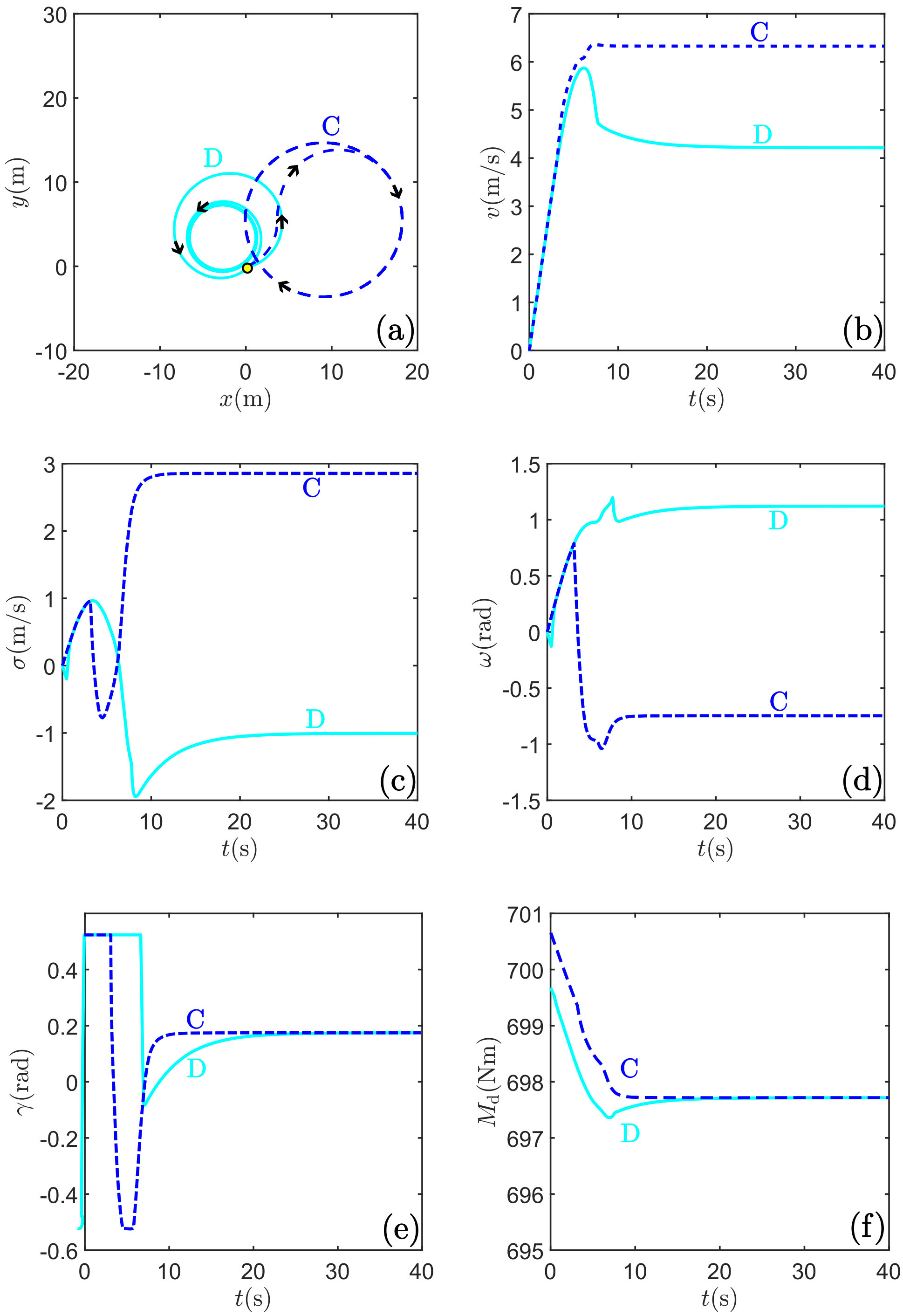

Figure 14. Simulation result for stabilizing the drifting solution C and the donut solution D.

engaged and then the steering angle converges to the negative steering angle that is of the same magnitude as was used to maintain the donut.

Finally, we demonstrate the flexibility of our control framework in creating a large variety of different extreme maneuvers. We take advantage of the different donut and drifting states unveiled by the bifurcation analysis and the simplicity (and consequently

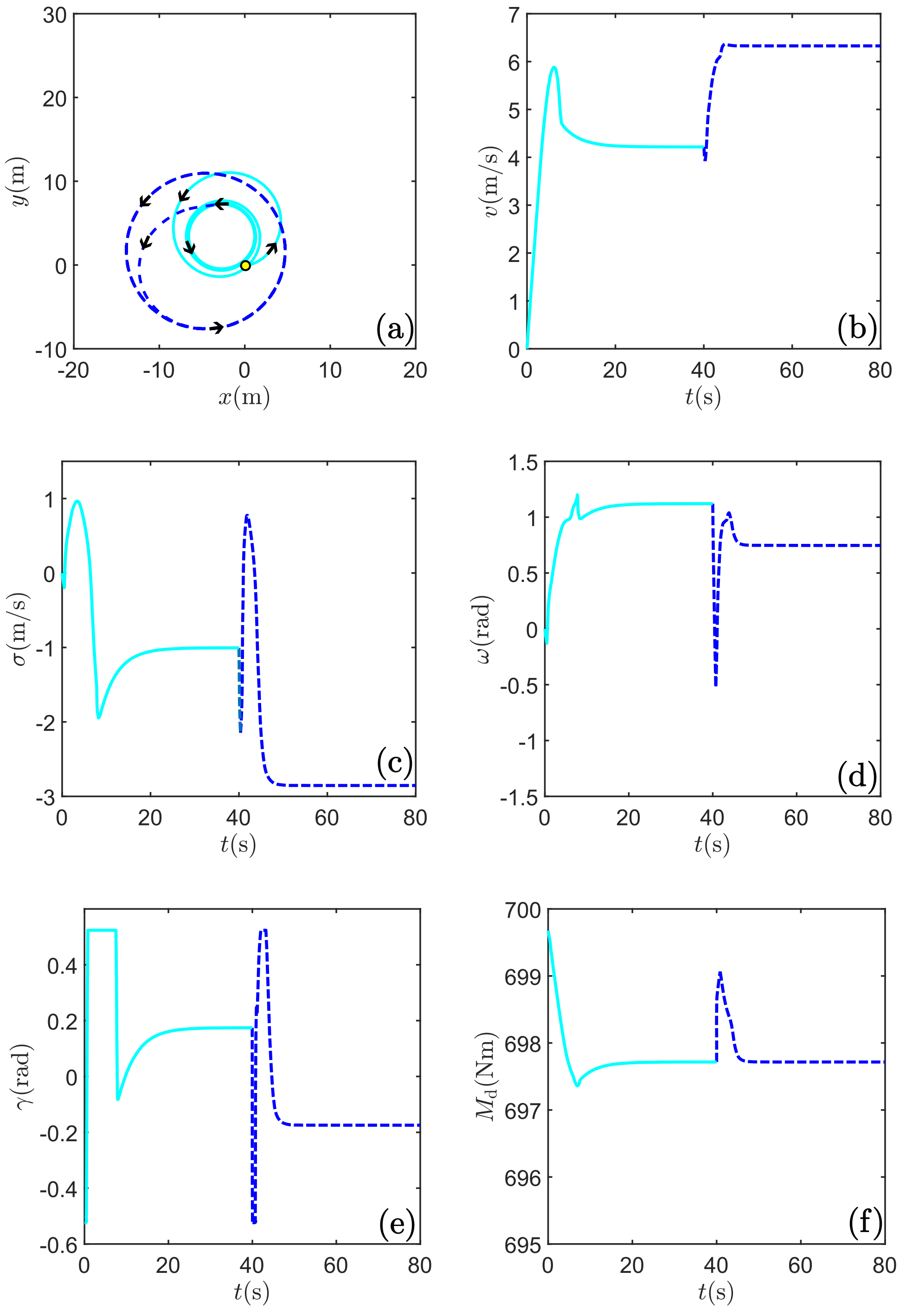

Figure 15. Simulation result when transitioning from donut to drifting by switching controllers.

low computational need) of our control design. The simulation results in Figure 16 combine a figure eight donut with a figure eight drifting. Starting from standstill, the vehicle first activates the counterclockwise donut controller and approaches the corresponding steady state, see the small-radius cyan circle in the top right of Figure 16(a). Then, at time 30 s, we switch to the clockwise donut controller, which transitions the

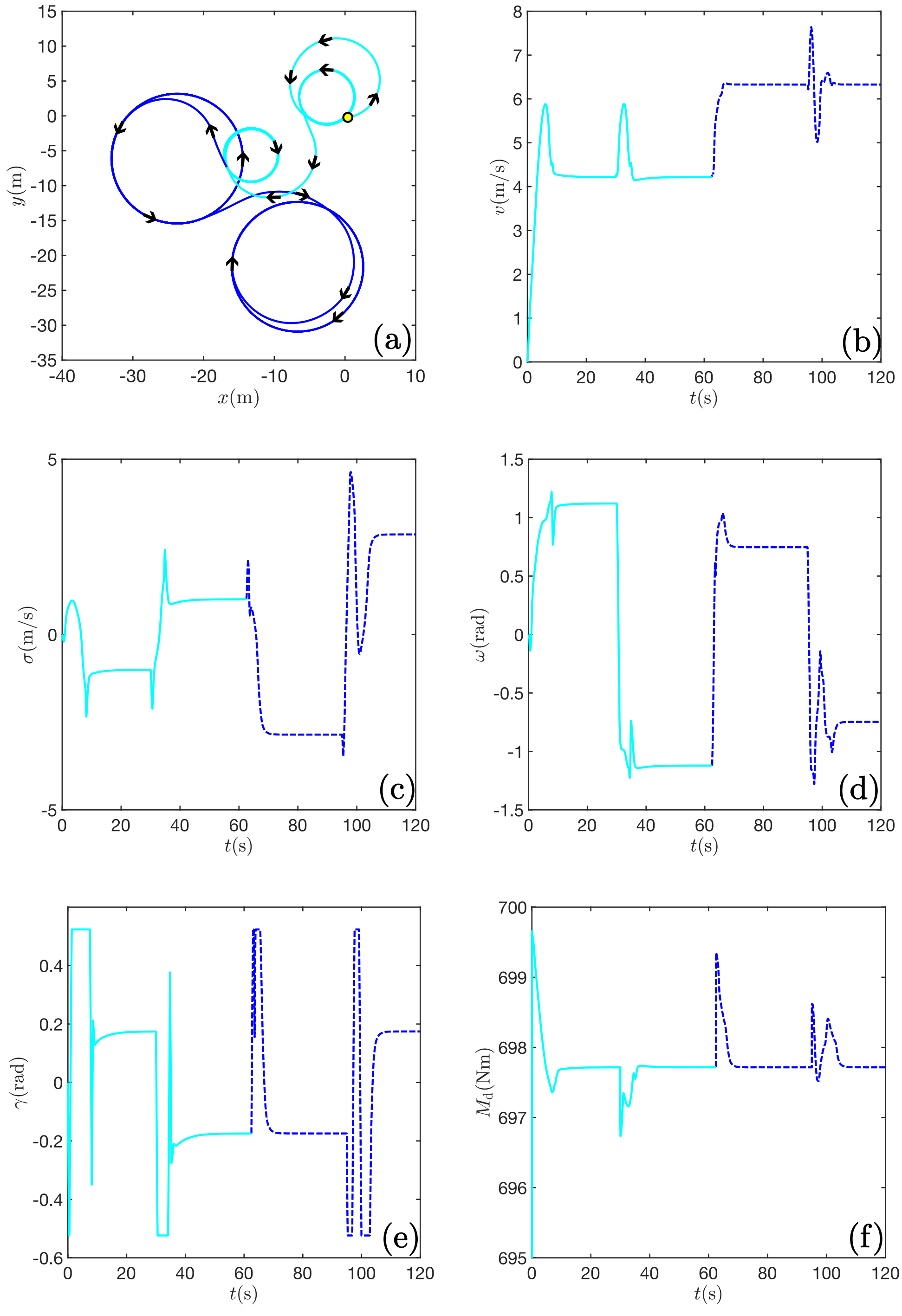

Figure 16. Simulation result when transitioning from donut figure eight maneuver to drifting figure eight maneuver by switching between four different controllers.

vehicle to the corresponding steady state. This is followed by a switch to the counterclockwise drifting controller at time 62.5 s that results in the transition from the small-radius cyan circle in the middle to the large-radius dark blue circle on the left. Finally, at time 95 s, the clockwise drifting controller is activated, and accordingly, the vehicle approaches the large-radius dark blue circle at the bottom. While drifting-to-drifting figure eight maneuvers have been explored before in the literature, our simulation shows that many other extreme transitions are possible. This enables turns with smaller turning radii: even during the transients between counterclockwise and clockwise donuts, the turning radius is significantly smaller than during drifting.

Overall, the ability to switch between the donut motion and the drifting motion can provide more flexibility in utilizing both the high speed nature of the drifting motion and the tighter cornering of the donut motion during extreme maneuvers. We also remark that the high-fidelity nature of the vehicle model with the wheel speed dynamics and combined slip tires plays a key enabler for the simple state feedback controllers to realize such complicated maneuvers.

6. Conclusion

We utilized state-of-the-art modeling and analysis techniques in order to gain a better understanding of the nonlinear dynamics of automated vehicles. We exploited the Appellian approach to build the 5 DoF vehicle model, which was supported by a combined slip tire model. This way, we included the dynamics of the wheel rotations while keeping the simplicity of the model. By using bifurcation analysis we explored the dynamics of the uncontrolled system and mapped out the dynamics around three important steady states (steady state cornering, donut, drifting), including the arising periodic solutions, which bifurcate from these steady states.

We showed that stable steady-state cornering appears for small driving torque inputs and they transform into an unstable donut through a series of bifurcations. First, stability is lost via Hopf bifurcation, which also results in periodic orbits of initially small amplitude. Then the longitudinal speed drops and the yaw rate rises through two fold bifurcations. We also showed that drifting is always unstable and appears through a singularity as the driving torque is increased. Moreover, the symmetric copy of the drifting state (for negative steering angle) is close to the donut state, which suggests that one may transition the vehicle between these states using appropriate control actions.

We demonstrated that the unstable donut and drifting states can be stabilized by simple, computationally inexpensive controllers and that one may indeed transition the vehicle between these states by switching the controller. This will enable automated vehicles to execute safety critical maneuvers, which they were unable to do previously. The designed controllers are, in principle, deployable on vehicles of different levels of automation but indeed the actual algorithms may depend on the automation level, which we plan to explore in the future. Another important factor, which will be the subject of future investigations, is the time delay in the control loops, as this can significantly influence the vehicle's motion in many scenarios. Finally, we are planning to validate our control framework using real vehicles on a test track.

Acknowledgements

DT would also like to thank the Rosztoczy Foundation for their generous support. GO acknowledges the support of the Hungarian Academy of Sciences within the Distinguished Guest Fellowship Programme and the support of a Fulbright Fellowship. The authors would also like to thank Chris Gerdes for the insightful discussions.

References

[1] Ersal T, Kolmanovsky I, Masoud N, et al. Connected and automated road vehicles: state of the art and future challenges. Vehicle System Dynamics. 2020;58(5):672–704.

[2] Talvala KLR, Kritayakirana K, Gerdes JC. Pushing the limits: From lanekeeping to autonomous racing. Annual Reviews in Control. 2011;35(1):137–148.

[3] Kritayakirana K, Gerdes JC. Autonomous vehicle control at the limits of handling. International Journal of Vehicle Autonomous Systems. 2012;10(4):271–296.

[4] Tavernini D, Massaro M, Velenis E, et al. Minimum time cornering: the effect of road surface and car transmission layout. Vehicle System Dynamics. 2013;51(10):1533–1547.

[5] Velenis E, Katzourakis D, Frazzoli E, et al. Steady-state drifting stabilization of rwd vehicles. Control Engineering Practice. 2011;19(11):1363–1376.

[6] Liu J, Jayakumar P, Stein JL, et al. A nonlinear model predictive control formulation for obstacle avoidance in high-speed autonomous ground vehicles in unstructured environments. Vehicle System Dynamics. 2018;56(6):853–882.

[7] Li SE, Chen H, Li R, et al. Predictive lateral control to stabilise highly automated vehicles at tire-road friction limits. Vehicle System Dynamics. 2020;58(5):768–786.

[8] Hu C, Zhou X, Duo R, et al. Combined fast control of drifting state and trajectory tracking for autonomous vehicles based on mpc controller. In: International Conference on Robotics and Automation (ICRA); IEEE; 2022. p. 1373–1379.

[9] Yang B, Lu Y, Yang X, et al. A hierarchical control framework for drift maneuvering of autonomous vehicles. In: International Conference on Robotics and Automation (ICRA); IEEE; 2022. p. 1387–1393.

[10] Goh JYM, Goel T, Gerdes JC. Toward automated vehicle control beyond the stability limits: drifting along a general path. Journal on Dynamic Systems Measurement and Control. 2020;142(2):021004.

[11] Peterson MT, Goel T, Gerdes JC. Exploiting linear structure for precision control of highly nonlinear vehicle dynamics. IEEE Transactions on Intelligent Vehicles. 2023;8(2):1852–1862.

[12] Goh JYM, Thompson M, Dallas J, et al. Beyond the stable handling limits: nonlinear model predictive control for highly transient autonomous drifting. Vehicle System Dynamics. 2024;62(10):2590–2613.

[13] Weber TP, Gerdes JC. Modeling and control for dynamic drifting trajectories. IEEE Transactions on Intelligent Vehicles. 2024;9(2):3731–3741.

[14] Dallas J, Talbot J, Suminaka M, et al. Control barrier functions for shared control and vehicle safety. In: American Control Conference; 2025. p. arXiv:2503.19994.

[15] Edelmann J, Plöchl M. Analysis of controllability of automobiles at steady-state cornering considering different drive concepts. In: The dynamics of vehicles on roads and tracks. CRC Press; 2017. p. 3–8.

[16] Bobier-Tiu CG, Beal CE, Kegelman JC, et al. Vehicle control synthesis using phase portraits of planar dynamics. Vehicle System Dynamics. 2019;57(9):1318–1337.

[17] Steindl A, Edelmann J, Plöchl M. Limit cycles at oversteer vehicle. Nonlinear Dynamics. 2020;99:313–321.

[18] Oh S, Avedisov SS, Orosz G. On the handling of automated vehicles: Modeling, bifurcation analysis, and experiments. European Journal of Mechanics A. 2021;90:104372.

[19] Vörös I, Takács D, Orosz G. Safe lane-keeping with feedback delay: bifurcation analysis and experiments. IEEE Control Systems Letters. 2023;7:1147–1152.

[20] Beal CE, Boyd C. Coupled lateral-longitudinal vehicle dynamics and control design with three-dimensional state portraits. Vehicle System Dynamics. 2019;57(2):286–313.

[21] Milani S, Marzbani H, Jazar RN. Vehicle drifting dynamics: discovery of new equilibria. Vehicle System Dynamics. 2021;60(6):1933–1958.

[22] Della Rossa F, Mastinu G, Piccardi C. Bifurcation analysis of an automobile model negotiating a curve. Vehicle System Dynamics. 2012;50(10):1539–1562.

[23] Vörös I, Orosz G, Takács D. On the global dynamics of path-following control of auto-

mated passenger vehicles. Nonlinear Dynamics. 2023;111(9):8235–8252.
[24] Rankin J, Coetzee E, Krauskopf B, et al. Bifurcation and stability analysis of aircraft turning on the ground. Journal of Guidance, Control, and Dynamics. 2009;32(2):500–511.
[25] Fiala E. Seitenkräfte am rollenden Luftreifen (Lateral forces on the rolling pneumatic tire). Zeitschrift der Vereines Deutscher Ingenieure (Magazine of the Association of German Engineers). 1954;96:973–979.
[26] Lu H, Stepan G, Lu J, et al. Dynamics of vehicle stability control subjected to feedback delay. European Journal of Mechanics A. 2022;96:104678.
[27] Beregi S, Avedisov SS, He CR, et al. Connectivity-based delay-tolerant control of automated vehicles: theory and experiments. IEEE Transactions on Intelligent Vehicles. 2023; 8(1):275–289.
[28] Pacejka H. Tire and vehicle dynamics. Elsevier; 2005.
[29] Djeumou F, Goh JY, Topcu U, et al. Autonomous drifting with 3 minutes of data via learned tire models. In: IEEE International Conference on Robotics and Automation (ICRA); IEEE; 2023. p. 968–974.
[30] Abdulrahim M. On the dynamics of automobile drifting. In: SAE World Congress; 2006. p. 2006–01–1019.
[31] Zhuang Y, Song Z, Gao X, et al. A combined-slip physical tire model based on the vector distribution considering tire anisotropic stiffness. Nonlinear Dynamics. 2022;108(4):2961–2976.
[32] Svendenius J, Gäfvert M. A brush-model based semi-empirical tire-model for combined slips. In: SAE World Congress; 2004. p. 2004–01–1064.
[33] Mastinu G, Biggio D, Della Rossa F, et al. Straight running stability of automobiles: experiments with a driving simulator. Nonlinear Dynamics. 2020;99(4):2801–2818.
[34] Steindl A, Edelmann J, Plöchl M. Influence of tyre characteristics on periodic motions for an understeering vehicle. PAMM. 2023;22(1):e202200289.
[35] Gibbs JW. On the fundamental formulae of dynamics. American Journal of Mathematics. 1879;2(1):49–64.
[36] Appell P. Sur une forme générale des équations de la dynamique (On a general form of the equations of dynamics). Journal für die reine und angewandte Mathematik (Journal for Pure and Applied Mathematics). 1900;121:310–319.
[37] Gantmacher F. Lectures in analytical mechanics. MIR Publishers, Moscow; 1970.
[38] Kane TR, Levinson DA. Dynamics, theory and applications. McGraw-Hill; 1985.
[39] De Sapio V. Advanced analytical dynamics: Theory and applications. Cambridge University Press; 2017.
[40] Antali M, Stepan G. Nonsmooth analysis of three-dimensional slipping and rolling in the presence of dry friction. Nonlinear Dynamics. 2019;97:1799–1817.
[41] Antali M, Stepan G. On the nonsmooth dynamics of towed wheels. Meccanica. 2020; 55(12):2523–2540.
[42] Qin WB, Zhang Y, Takács D, et al. Nonholonomic dynamics and control of road vehicles: moving toward automation. Nonlinear Dynamics. 2022;110(3):1959–2004.
[43] Engelborghs K, Luzyanina T, Samaey G. DDE-BIFTOOL v. 2.00: a matlab package for bifurcation analysis of delay differential equations. TW Reports. 2001;:61–61.
[44] Sieber J, Engelborghs K, Luzyanina T, et al. DDE-BIFTOOL manual-bifurcation analysis of delay differential equations. arXiv preprint arXiv:14067144. 2014;.
[45] Oh S, Avedisov SS, Orosz G. On the handling of automated vehicles: Modeling, bifurcation analysis, and experiments. European Journal of Mechanics A. 2021;90:104372.
[46] Bachrathy D, Stépán G. Bisection method in higher dimensions and the efficiency number. Periodica Polytechnica. 2012;56(2):81–86.
[47] Bernard JE, Segel L, Wild RE. Tire shear force generation during combined steering and braking maneuvers. SAE Transactions. 1977;86:2953–2969.

Appendix A. The 5 DoF Single Track Model (Detailed Derivation)

Here we show the derivation of the equations of motion for our 5 DoF single track model discussed in Section 3.1 using the Appellian approach. The mechanical model is illustrated in Figure 4 and the system parameters are collected in Table 1.

In order to describe the mechanical system we need five generalized coordinates and here we choose $x_{\rm G}, y_{\rm G}, \psi, \theta_{\rm r}, \theta_{\rm f}$. The Appellian approach requires the introduction of the so-called pseudo velocities, which can be chosen intuitively. One can formulate the velocity of the center of mass G both in the ground-fixed frame $\rm F_0$ and in the vehicle-fixed frame $\rm F_1$:

$$\mathbf{v}_{\rm G} = \begin{bmatrix} \dot{x}_{\rm G} \\ \dot{y}_{\rm G} \\ 0 \end{bmatrix}_{\rm F_0}, \qquad \mathbf{v}_{\rm G} = \begin{bmatrix} \dot{x}_{\rm G}\cos\psi + \dot{y}_{\rm G}\sin\psi \\ -\dot{x}_{\rm G}\sin\psi + \dot{y}_{\rm G}\cos\psi \\ 0 \end{bmatrix}_{\rm F_1}. \tag{A1}$$

One may also formulate the angular velocity vector of the vehicle body as

$$\boldsymbol{\omega}_{\rm v} = \begin{bmatrix} 0 \\ 0 \\ \dot{\psi} \end{bmatrix}_{\rm F_0}, \qquad \boldsymbol{\omega}_{\rm v} = \begin{bmatrix} 0 \\ 0 \\ \dot{\psi} \end{bmatrix}_{\rm F_1}, \tag{A2}$$

which will be used in the calculations below.

Using the longitudinal and later velocity components $v := \dot{x}_{\rm G}\cos\psi + \dot{y}_{\rm G}\sin\psi$ and $\sigma := -\dot{x}_{\rm G}\sin\psi + \dot{y}_{\rm G}\cos\psi$ together with the angular velocity components $\omega := \dot{\psi}$, $\Omega_{\rm r} := \dot{\theta}_{\rm r}$ and $\Omega_{\rm f} := \dot{\theta}_{\rm f}$ as pseudo velocities, we obtain the linear system

$$\begin{bmatrix} \cos\psi & \sin\psi & 0 & 0 & 0 \\ -\sin\psi & \cos\psi & 0 & 0 & 0 \\ 0 & 0 & 1 & 0 & 0 \\ 0 & 0 & 0 & 1 & 0 \\ 0 & 0 & 0 & 0 & 1 \end{bmatrix} \begin{bmatrix} \dot{x}_{\rm G} \\ \dot{y}_{\rm G} \\ \dot{\psi} \\ \dot{\theta}_{\rm r} \\ \dot{\theta}_{\rm f} \end{bmatrix} = \begin{bmatrix} v \\ \sigma \\ \omega \\ \Omega_{\rm r} \\ \Omega_{\rm f} \end{bmatrix}. \tag{A3}$$

Since the matrix on the left hand side is not singular (its determinant is 1), one may solve the linear equations and obtain

$$\begin{aligned} \dot{x}_{\rm G} &= v\cos\psi - \sigma\sin\psi\,, \\ \dot{y}_{\rm G} &= v\sin\psi + \sigma\cos\psi\,, \\ \dot{\psi} &= \omega\,, \\ \dot{\theta}_{\rm r} &= \Omega_{\rm r}\,, \\ \dot{\theta}_{\rm f} &= \Omega_{\rm f}\,, \end{aligned} \tag{A4}$$

which is identical to (6).

Note that since there are no kinematic constraint the number of pseudo-velocities are the same as the number of generalized velocities [42]. Still the advantage of the Appellian approach is that it allows one to describe the configuration of the system in the ground-fixed frame (using the generalized coordinates), and at the same time describe the velocity state of the system in the body-fixed frame (using the pseudo velocities).

Similar to the Lagrangian approach, which uses the kinetic energy of the multi-body system, the Appellian approach is relies on a scalar quantity called the acceleration energy. This can be constructed as

$$S = S_{\mathrm{veh}} + S_{\mathrm{fw}} + S_{\mathrm{rw}}, \tag{A5}$$

where S_{veh}, S_{rw} and S_{fw} are the acceleration energies of the vehicle body, the rear wheel and the front wheel, respectively. These can be calculated as

$$S_{\mathrm{veh}} = \frac{1}{2} m_{\mathrm{v}} \mathbf{a}_{\mathrm{G}}^2 + \frac{1}{2} J_{\mathrm{G}} \boldsymbol{\alpha}_{\mathrm{v}}^2 + \ldots, \tag{A6}$$

$$S_{\mathrm{rw}} = \frac{1}{2} m_{\mathrm{w}} \mathbf{a}_{\mathrm{R}}^2 + \frac{1}{2} \boldsymbol{\alpha}_{\mathrm{r}} \cdot \mathbf{J}_{\mathrm{R}} \boldsymbol{\alpha}_{\mathrm{r}} + \boldsymbol{\alpha}_{\mathrm{r}} \cdot (\boldsymbol{\omega}_{\mathrm{r}} \times \mathbf{J}_{\mathrm{R}} \boldsymbol{\omega}_{\mathrm{r}}) + \ldots, \tag{A7}$$

$$S_{\mathrm{fw}} = \frac{1}{2} m_{\mathrm{w}} \mathbf{a}_{\mathrm{F}}^2 + \frac{1}{2} \boldsymbol{\alpha}_{\mathrm{f}} \cdot \mathbf{J}_{\mathrm{F}} \boldsymbol{\alpha}_{\mathrm{f}} + \boldsymbol{\alpha}_{\mathrm{f}} \cdot (\boldsymbol{\omega}_{\mathrm{f}} \times \mathbf{J}_{\mathrm{F}} \boldsymbol{\omega}_{\mathrm{f}}) + \ldots, \tag{A8}$$

where $\mathbf{a}_{\mathrm{G}}$, $\mathbf{a}_{\mathrm{R}}$ and $\mathbf{a}_{\mathrm{F}}$ are the acceleration vectors of the points G, R and F, respectively, $\boldsymbol{\alpha}_{\mathrm{v}}$, $\boldsymbol{\alpha}_{\mathrm{r}}$ and $\boldsymbol{\alpha}_{\mathrm{f}}$ are the angular acceleration vectors of the vehicle body, the rear wheel and the front wheel, respectively, while $\boldsymbol{\omega}_{\mathrm{r}}$ and $\boldsymbol{\omega}_{\mathrm{f}}$ are the angular velocity vectors of the rear wheel and the front wheel, respectively. Moreover, m_{v} is the mass of the vehicle, m_{w} denotes the mass of the wheels, while the mass moment of inertia tensors of the wheels at the wheel center points R and F (in the appropriate frames) are

$$\mathbf{J}_{\mathrm{R}} = \begin{bmatrix} C & 0 & 0 \\ 0 & D & 0 \\ 0 & 0 & C \end{bmatrix}_{\mathrm{F}_1}, \quad \text{and} \quad \mathbf{J}_{\mathrm{F}} = \begin{bmatrix} C & 0 & 0 \\ 0 & D & 0 \\ 0 & 0 & C \end{bmatrix}_{\mathrm{F}_2}. \tag{A9}$$

Note that the expression of the acceleration energy S_{veh} in (A6) is simpler than those of S_{rw} and S_{fw} in (A7) and (A8), because the vehicle body executes an in-plane motion while the wheels are performing spatial motions. Finally, $\ldots$ denotes additional terms which are not spelled out since they do not contain acceleration components.

The acceleration energy needs to be expressed as functions of pseudo velocities $v, \sigma, \omega, \Omega_{\mathrm{r}}, \Omega_{\mathrm{f}}$ and the pseudo accelerations $\dot{v}, \dot{\sigma}, \dot{\omega}, \dot{\Omega}_{\mathrm{r}}, \dot{\Omega}_{\mathrm{f}}$. Taking the time derivative of (A4) yields

$$\begin{aligned} \ddot{x}_{\mathrm{G}} &= \dot{v}\cos\psi - v\omega\sin\psi - \dot{\sigma}\sin\psi - \sigma\omega\cos\psi\,, \\ \ddot{y}_{\mathrm{G}} &= \dot{v}\sin\psi + v\omega\cos\psi + \dot{\sigma}\cos\psi - \sigma\omega\sin\psi\,, \\ \ddot{\psi} &= \dot{\omega}\,, \\ \ddot{\theta}_{\mathrm{r}} &= \dot{\Omega}_{\mathrm{r}}\,, \\ \ddot{\theta}_{\mathrm{f}} &= \dot{\Omega}_{\mathrm{f}}\,. \end{aligned} \tag{A10}$$

Next, we present the calculation of the acceleration energy for each rigid body. For the vehicle body the acceleration and the angular acceleration vectors can be expressed in the ground-fixed frame F_0:

$$\mathbf{a}_{\mathrm{G}} = \dot{\mathbf{v}}_{\mathrm{G}} = \begin{bmatrix} \ddot{x}_{\mathrm{G}} \\ \ddot{y}_{\mathrm{G}} \\ 0 \end{bmatrix}_{\mathrm{F}_0}, \qquad \boldsymbol{\alpha}_{\mathrm{v}} = \dot{\boldsymbol{\omega}}_{\mathrm{v}} = \begin{bmatrix} 0 \\ 0 \\ \ddot{\psi} \end{bmatrix}_{\mathrm{F}_0}, \tag{A11}$$

cf. (A1) and (A2). Using (A10), results in

$$\mathbf{a}_{\mathrm{G}}^2 = \dot{v}^2 + \dot{\sigma}^2 - 2\omega\sigma\dot{v} + 2\omega v\dot{\sigma} + \ldots\,, \qquad \boldsymbol{\alpha}_{\mathrm{v}}^2 = \dot{\omega}^2\,, \tag{A12}$$

and substituting these into (A6) yields

$$S_{\mathrm{veh}} = \frac{1}{2}m_{\mathrm{v}}\dot{v}^2 + \frac{1}{2}m_{\mathrm{v}}\dot{\sigma}^2 + \frac{1}{2}J_{\mathrm{G}}\dot{\omega}^2 - m_{\mathrm{v}}\omega\sigma\dot{v} + m_{\mathrm{v}}\omega v\dot{\sigma} + \ldots\,. \tag{A13}$$

Again $\ldots$ represent terms which do not contain the pseudo accelerations $\dot{v}$ or $\dot{\sigma}$ as these will play no role in the Appell equations derived below.

For the rear wheel one may calculate the acceleration of the wheel center point R using the transport formula

$$\mathbf{a}_{\mathrm{R}} = \mathbf{a}_{\mathrm{G}} + \boldsymbol{\alpha}_{\mathrm{v}} \times \mathbf{r}_{\mathrm{GR}} + \boldsymbol{\omega}_{\mathrm{v}} \times (\boldsymbol{\omega}_{\mathrm{v}} \times \mathbf{r}_{\mathrm{GR}}) = \begin{bmatrix} \ddot{x}_{\mathrm{G}} + d\dot{\omega}\sin\psi + d\omega^2\cos\psi \\ \ddot{y}_{\mathrm{G}} - d\dot{\omega}\cos\psi + d\omega^2\sin\psi \\ 0 \end{bmatrix}_{\mathrm{F}_0}, \tag{A14}$$

where we used (A2), (A4), (A11) and the position vector $\mathbf{r}_{\mathrm{GR}} = [\,-d\cos\psi \;\; -d\sin\psi \;\; 0\,]_{\mathrm{F}_0}^{\mathrm{T}}$ pointing from G to R. Again, using (A10) yields

$$\mathbf{a}_{\mathrm{R}}^2 = \dot{v}^2 + \dot{\sigma}^2 + d^2\dot{\omega}^2 - 2d\dot{\sigma}\dot{\omega} - 2dv\omega\dot{\omega} + 2d\omega^2\dot{v} - 2\omega\sigma\dot{v} + 2\omega v\dot{\sigma} + \ldots\,. \tag{A15}$$

The angular velocity vector of the rear wheel can be formulated conveniently in the frame F_1:

$$\boldsymbol{\omega}_{\mathrm{r}} = \begin{bmatrix} 0 \\ \Omega_{\mathrm{r}} \\ \omega \end{bmatrix}_{\mathrm{F}_1}, \tag{A16}$$

which, using the concept of frame derivatives, leads to

$$\boldsymbol{\alpha}_{\mathrm{r}} = \dot{\boldsymbol{\omega}}_{\mathrm{r}} = \begin{bmatrix} -\omega\Omega_{\mathrm{r}} \\ \dot{\Omega}_{\mathrm{r}} \\ \dot{\omega} \end{bmatrix}_{\mathrm{F}_1}. \tag{A17}$$

Then, using (A9), (A16), (A17), we obtain

$$\frac{1}{2}\boldsymbol{\alpha}_{\mathrm{r}} \cdot \mathbf{J}_{\mathrm{R}}\boldsymbol{\alpha}_{\mathrm{r}} + \boldsymbol{\alpha}_{\mathrm{r}} \cdot (\boldsymbol{\omega}_{\mathrm{r}} \times \mathbf{J}_{\mathrm{R}}\boldsymbol{\omega}_{\mathrm{r}}) = \frac{1}{2}C\dot{\omega}^2 + \frac{1}{2}D\dot{\Omega}_{\mathrm{r}}^2 + \ldots\,. \tag{A18}$$

Substituting (A15) and (A18) into (A7) we obtain

$$\begin{aligned} S_{\mathrm{rw}} = {} & \frac{1}{2}m_{\mathrm{w}}\dot{v}^2 + \frac{1}{2}m_{\mathrm{w}}\dot{\sigma}^2 + \frac{1}{2}\big(m_{\mathrm{w}}d^2 + C\big)\dot{\omega}^2 + \frac{1}{2}D\dot{\Omega}_{\mathrm{r}}^2 \\ & - m_{\mathrm{w}}d\dot{\sigma}\dot{\omega} - m_{\mathrm{w}}dv\omega\dot{\omega} + m_{\mathrm{w}}d\omega^2\dot{v} - m_{\mathrm{w}}\omega\sigma\dot{v} + m_{\mathrm{w}}v\omega\dot{\sigma} + \ldots\,. \end{aligned} \tag{A19}$$

Taking a similar approach for the front wheel, the acceleration of the wheel center point F can be calculated as

$$\mathbf{a}_{\mathrm{F}} = \mathbf{a}_{\mathrm{G}} + \boldsymbol{\alpha}_{\mathrm{v}} \times \mathbf{r}_{\mathrm{GF}} + \boldsymbol{\omega}_{\mathrm{v}} \times (\boldsymbol{\omega}_{\mathrm{v}} \times \mathbf{r}_{\mathrm{GF}}) = \begin{bmatrix} \ddot{x}_{\mathrm{G}} - q\dot{\omega}\sin\psi - q\omega^2\cos\psi \\ \ddot{y}_{\mathrm{G}} + q\dot{\omega}\cos\psi - q\omega^2\sin\psi \\ 0 \end{bmatrix}_{\mathrm{F}_0}, \tag{A20}$$

where we used (A2), (A4), (A11) and the position vector $\mathbf{r}_{\mathrm{GF}} = [\, q\cos\psi \quad q\sin\psi \quad 0\,]^{\top}_{\mathrm{F}_0}$ pointing from G to F. Again, using (A10) yields

$$\mathbf{a}_{\mathrm{F}}^2 = \dot{v}^2 + \dot{\sigma}^2 + q^2\dot{\omega}^2 + 2q\dot{\sigma}\dot{\omega} + 2qv\omega\dot{\omega} - 2q\omega^2\dot{v} - 2\omega\sigma\dot{v} + 2\omega v\dot{\sigma} + \dots\,. \tag{A21}$$

The angular velocity vector of the front wheel can be formulated conveniently in the frame F_2:

$$\boldsymbol{\omega}_{\mathrm{f}} = \begin{bmatrix} 0 \\ \Omega_{\mathrm{f}} \\ \omega + \dot{\gamma} \end{bmatrix}_{\mathrm{F}_2}, \tag{A22}$$

and using frame derivatives we obtain

$$\boldsymbol{\alpha}_{\mathrm{f}} = \dot{\boldsymbol{\omega}}_{\mathrm{f}} = \begin{bmatrix} -\omega(\Omega_{\mathrm{f}} + \dot{\gamma}) \\ \dot{\Omega}_{\mathrm{f}} \\ \dot{\omega} + \ddot{\gamma} \end{bmatrix}_{\mathrm{F}_2}. \tag{A23}$$

Then, using (A9), (A22), (A23), we obtain

$$\frac{1}{2}\boldsymbol{\alpha}_{\mathrm{f}} \cdot \mathbf{J}_{\mathrm{R}}\boldsymbol{\alpha}_{\mathrm{f}} + \boldsymbol{\alpha}_{\mathrm{f}} \cdot (\boldsymbol{\omega}_{\mathrm{f}} \times \mathbf{J}_{\mathrm{F}}\boldsymbol{\omega}_{\mathrm{f}}) = \frac{1}{2}C\big(\dot{\omega}^2 + 2\ddot{\gamma}\dot{\omega}\big) + \frac{1}{2}D\dot{\Omega}_{\mathrm{f}}^2 + \dots\,. \tag{A24}$$

Substituting (A21) and (A24) into (A8), we obtain

$$\begin{aligned} S_{\mathrm{fw}} = {} & \frac{1}{2}m_{\mathrm{w}}\dot{v}^2 + \frac{1}{2}m_{\mathrm{w}}\dot{\sigma}^2 + \frac{1}{2}\big(m_{\mathrm{w}}q^2 + C\big)\dot{\omega}^2 + C\ddot{\gamma}\dot{\omega} + \frac{1}{2}D\dot{\Omega}_{\mathrm{f}}^2 \\ & + m_{\mathrm{w}}q\dot{\sigma}\dot{\omega} + m_{\mathrm{w}}qv\omega\dot{\omega} - m_{\mathrm{w}}q\omega^2\dot{v} - m_{\mathrm{w}}\omega\sigma\dot{v} + m_{\mathrm{w}}\omega v\dot{\sigma} + \dots\,. \end{aligned} \tag{A25}$$

Finally, substituting (A13), (A19), (A25) into (A5) we obtain

$$\begin{aligned} S = {} & \frac{1}{2}m\dot{v}^2 + \frac{1}{2}m\dot{\sigma}^2 + \frac{1}{2}J\dot{\omega}^2 + \frac{1}{2}D\dot{\Omega}_{\mathrm{r}}^2 + \frac{1}{2}D\dot{\Omega}_{\mathrm{f}}^2 \\ & + p\dot{\sigma}\dot{\omega} - (p\omega^2 + m\omega\sigma)\dot{v} + m\omega v\dot{\sigma} + (C\ddot{\gamma} + pv\omega)\dot{\omega} + \dots, \end{aligned} \tag{A26}$$

where

$$\begin{aligned} m &= m_{\mathrm{v}} + 2m_{\mathrm{w}}, \\ p &= m_{\mathrm{w}}(q - d), \\ J &= J_{\mathrm{G}} + m_{\mathrm{w}}\big(d^2 + q^2\big) + 2C. \end{aligned} \tag{A27}$$

cf. (8).

Beside the acceleration energy, we also need to calculate the so-called pseudo forces. These can be obtained by calculating the virtual power of the active forces, which are the tire forces and the aligning moments and the driving torque:

$$\delta P = \mathbf{F}_{\mathrm{r}} \cdot \delta \mathbf{v}_{\mathrm{A}} + (\mathbf{M}_{\mathrm{r}} + \mathbf{M}_{\mathrm{d}}) \cdot \delta \boldsymbol{\omega}_{\mathrm{r}} + \mathbf{F}_{\mathrm{f}} \cdot \delta \mathbf{v}_{\mathrm{B}} + \mathbf{M}_{\mathrm{f}} \cdot \delta \boldsymbol{\omega}_{\mathrm{f}} \,, \tag{A28}$$

where $\mathbf{v}_{\mathrm{A}}$ and $\mathbf{v}_{\mathrm{B}}$ are the velocities of points where the tire forces act on the wheel; see Figure 4. For the rear wheel, it is convenient to resolve the forces and the torques in the F_1 frame:

$$\mathbf{F}_{\mathrm{r}} = \begin{bmatrix} F_{x,\mathrm{r}} \\ F_{y,\mathrm{r}} \\ 0 \end{bmatrix}_{\mathrm{F}_1} \,, \quad \mathbf{M}_{\mathrm{r}} = \begin{bmatrix} 0 \\ 0 \\ M_{z,\mathrm{r}} \end{bmatrix}_{\mathrm{F}_1} \,, \quad \mathbf{M}_{\mathrm{d}} = \begin{bmatrix} 0 \\ M_{\mathrm{d}} \\ 0 \end{bmatrix}_{\mathrm{F}_1} \,, \tag{A29}$$

while for the front wheels, the frame F_2 is convenient:

$$\mathbf{F}_{\mathrm{f}} = \begin{bmatrix} F_{x,\mathrm{f}} \\ F_{y,\mathrm{f}} \\ 0 \end{bmatrix}_{\mathrm{F}_2} \,, \quad \mathbf{M}_{\mathrm{f}} = \begin{bmatrix} 0 \\ 0 \\ M_{z,\mathrm{f}} \end{bmatrix}_{\mathrm{F}_2} \,. \tag{A30}$$

The angular velocity vectors are already expressed in these frames (see (A2),(A16) and (A22)) while the velocities can be obtained using transport formulas:

$$\mathbf{v}_{\mathrm{R}} = \mathbf{v}_{\mathrm{G}} + \boldsymbol{\omega}_{\mathrm{v}} \times \mathbf{r}_{\mathrm{GR}} = \begin{bmatrix} v \\ \sigma - d\omega \\ 0 \end{bmatrix}_{\mathrm{F}_1} \,, \tag{A31}$$

$$\mathbf{v}_{\mathrm{A}} = \mathbf{v}_{\mathrm{R}} + \boldsymbol{\omega}_{\mathrm{r}} \times \mathbf{r}_{\mathrm{RA}} = \begin{bmatrix} v - r\Omega_{\mathrm{r}} \\ \sigma - d\omega \\ 0 \end{bmatrix}_{\mathrm{F}_1} \,, \tag{A32}$$

$$\mathbf{v}_{\mathrm{F}} = \mathbf{v}_{\mathrm{G}} + \boldsymbol{\omega}_{\mathrm{v}} \times \mathbf{r}_{\mathrm{GF}} = \begin{bmatrix} v \\ \sigma + q\omega \\ 0 \end{bmatrix}_{\mathrm{F}_1} \quad \Rightarrow \quad \mathbf{v}_{\mathrm{F}} = \begin{bmatrix} v\cos\gamma + (\sigma + q\omega)\sin\gamma \\ -v\sin\gamma + (\sigma + q\omega)\cos\gamma \\ 0 \end{bmatrix}_{\mathrm{F}_2} \,, \tag{A33}$$

$$\mathbf{v}_{\mathrm{B}} = \mathbf{v}_{\mathrm{F}} + \boldsymbol{\omega}_{\mathrm{f}} \times \mathbf{r}_{\mathrm{FB}} = \begin{bmatrix} v\cos\gamma + (\sigma + q\omega)\sin\gamma - r\Omega_{\mathrm{f}} \\ -v\sin\gamma + (\sigma + q\omega)\cos\gamma \\ 0 \end{bmatrix}_{\mathrm{F}_2} \,, \tag{A34}$$

where we used the vectors $\mathbf{v}_{\mathrm{G}} = [\, v \;\; \sigma \;\; 0 \,]_{\mathrm{F}_1}^{\top}$ (cf. (A1)), $\mathbf{r}_{\mathrm{GR}} = [\, -d \;\; 0 \;\; 0 \,]_{\mathrm{F}_1}^{\top}$, $\mathbf{r}_{\mathrm{RA}} = [\, 0 \;\; 0 \;\; -r \,]_{\mathrm{F}_1}^{\top}$, $\mathbf{r}_{\mathrm{GF}} = [\, q \;\; 0 \;\; 0 \,]_{\mathrm{F}_1}^{\top}$, $\mathbf{r}_{\mathrm{FB}} = [\, 0 \;\; 0 \;\; -r \,]_{\mathrm{F}_2}^{\top}$.

Substituting (A16), (A22), (A29), (A30), (A31), (A33) into (A28) we obtain

$$\begin{aligned}\delta P = &F_{x,\mathrm{r}}\,\delta(v - r\Omega_\mathrm{r}) + F_{y,\mathrm{r}}\,\delta(\sigma - d\omega) + M_{z,\mathrm{r}}\,\delta\omega + M_\mathrm{d}\,\delta\Omega_\mathrm{r} \\ &+ F_{x,\mathrm{f}}\,\delta(v\cos\gamma + (\sigma + q\omega)\sin\gamma - r\Omega_\mathrm{f}) + F_{y,\mathrm{f}}\,\delta(-v\sin\gamma + (\sigma + q\omega)\cos\gamma) + M_{z,\mathrm{f}}\,\delta\omega\,,\end{aligned} \tag{A35}$$

where we used that $\delta\dot{\gamma} = 0$. Writing the virtual power into the form

$$\delta P = \Pi_v\,\delta v + \Pi_\sigma\,\delta\sigma + \Pi_\omega\,\delta\omega + \Pi_{\Omega_\mathrm{r}}\,\delta\Omega_\mathrm{r} + \Pi_{\Omega_\mathrm{f}}\,\delta\Omega_\mathrm{f}\,, \tag{A36}$$

the pseudo forces can be identified as

$$\begin{aligned}\Pi_v &= F_{x,\mathrm{r}} + F_{x,\mathrm{f}}\cos\gamma - F_{y,\mathrm{f}}\sin\gamma\,, \\ \Pi_\sigma &= F_{y,\mathrm{r}} + F_{x,\mathrm{f}}\sin\gamma + F_{y,\mathrm{f}}\cos\gamma\,, \\ \Pi_\omega &= -dF_{y,\mathrm{r}} + q(F_{x,\mathrm{f}}\sin\gamma + F_{y,\mathrm{f}}\cos\gamma) + M_{z,\mathrm{r}} + M_{z,\mathrm{f}}\,, \\ \Pi_{\Omega_\mathrm{r}} &= M_\mathrm{d} - rF_{x,\mathrm{r}}\,, \\ \Pi_{\Omega_\mathrm{f}} &= -rF_{x,\mathrm{f}}\,.\end{aligned} \tag{A37}$$

Finally, substituting the acceleration energy (A26) and the pseudo forces (A37) into the Appell equations

$$\begin{aligned}\frac{\partial S}{\partial \dot{v}} &= \Pi_v\,, \\ \frac{\partial S}{\partial \dot{\sigma}} &= \Pi_\sigma\,, \\ \frac{\partial S}{\partial \dot{\omega}} &= \Pi_\omega\,, \\ \frac{\partial S}{\partial \dot{\Omega}_\mathrm{r}} &= \Pi_{\Omega_\mathrm{r}}\,, \\ \frac{\partial S}{\partial \dot{\Omega}_\mathrm{f}} &= \Pi_{\Omega_\mathrm{f}}\,,\end{aligned} \tag{A38}$$

we can obtain the equations of motion:

$$\begin{aligned}\dot{v} &= \sigma\omega + \frac{1}{m}\big(p\omega^2 + F_{x,\mathrm{r}} + F_{x,\mathrm{f}}\cos\gamma - F_{y,\mathrm{f}}\sin\gamma\big), \\ \dot{\sigma} &= -v\omega + \frac{1}{Jm - p^2}\big((J + pd)F_{y,\mathrm{r}} + (J - pq)(F_{x,\mathrm{f}}\sin\gamma + F_{y,\mathrm{f}}\cos\gamma) \\ &\qquad - p(M_{z,\mathrm{r}} + M_{z,\mathrm{f}} - C\ddot{\gamma})\big), \\ \dot{\omega} &= \frac{1}{Jm - p^2}\big(-(md + p)F_{y,\mathrm{r}} + (mq - p)(F_{x,\mathrm{f}}\sin\gamma + F_{y,\mathrm{f}}\cos\gamma) \\ &\qquad + m(M_{z,\mathrm{r}} + M_{z,\mathrm{f}} - C\ddot{\gamma})\big), \\ \dot{\Omega}_\mathrm{r} &= \frac{1}{D}(M_\mathrm{d} - rF_{x,\mathrm{r}}), \\ \dot{\Omega}_\mathrm{f} &= \frac{1}{D}(-rF_{x,\mathrm{f}}),\end{aligned} \tag{A39}$$

which is identical with (7).

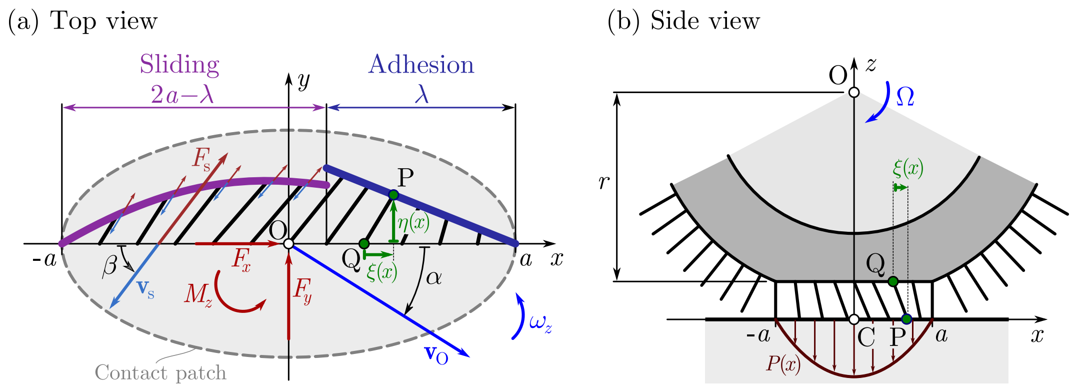

Figure B1. Combined slip brush tire model highlighting the adhesion region and the sliding region and indicating the slip angle α and the sliding angle β. The longitudinal and lateral tire deformations $\xi(x)$ and $\eta(x)$, the longitudinal and lateral tire forces F_x and F_y, and the aligning moment M_z are also shown on the figure.

Appendix B. Combined slip Brush Tire Model (Detailed Derivation)

In this section, we present the detailed derivation of the combined slip brush tire model, which was summarized in Section 3.2. As shown in Figure B1, the deformation of the tire within the contact patch is described in the (x, y, z) coordinate frame, which travels together with the wheel. The velocity of the wheel center is denoted by $\mathbf{v}_{\mathrm{O}}$ which forms a slip angle α with the wheel plane. In the meantime the wheel rotates with the angular velocity Ω around its axle. Note that point O takes the role of point R for the rear wheel and the role of point F for the front wheel in Figure 4. Similarly, point C takes the role of point A for the rear wheel and the role of point B for the front wheel in Figure 4. All vectors below are resolved in this moving coordinate frame which rotates around the z axis with angular velocity ω_z. Note that $\omega_z = \dot{\psi}$ for the rear wheel and $\omega_z = \dot{\psi} + \dot{\gamma}$ for the front wheel in Figure 4.

The brush elements deform along the contact line whose length is $2a$. Let us focus on a single element QP. Point Q is attached to the unstretchable band while point P touches the road surface and it either sticks to the ground (in which case it has zero velocity) or it slides on the ground. The longitudinal deformation of the brush element is denoted by $\xi(x, t)$, while the lateral deformation is denoted by $\eta(x, t)$; see Figure B1(a). These deformations depend on the longitudinal position x along the contact patch and time t. In addition, the pressure distribution along the contact patch is given by the parabola

$$p(x) = \frac{3F_z}{4aw}\left(1 - \frac{x^2}{a^2}\right) , \tag{B1}$$

where F_z is the normal force and w is the tire width; see Figure B1(b).

The position vector of point P can given as

$$\mathbf{r}_{\mathrm{OP}} = \begin{bmatrix} x + \xi(x, t) \\ \eta(x, t) \\ 0 \end{bmatrix} . \tag{B2}$$

Let us define the point P′ as a point fixed to the reference frame that coincides with P at a certain time instant. The velocity of P′ with respect to the road surface is $\mathbf{v}_{\mathrm{P,carr}}$ and the relative velocity of P with respect to the reference frame is $\mathbf{v}_{\mathrm{P,rel}}$. These can be written as:

$$\mathbf{v}_{\mathrm{P,carr}} = \mathbf{v}_{\mathrm{O}} + \boldsymbol{\omega} \times \mathbf{r}_{\mathrm{OP}} = \begin{bmatrix} v_{\mathrm{O}} \cos\alpha - \omega_z \eta(x,t) \\ -v_{\mathrm{O}} \sin\alpha + \omega_z x + \omega_z \xi(x,t) \\ 0 \end{bmatrix}, \tag{B3}$$

$$\mathbf{v}_{\mathrm{P,rel}} = \mathring{\mathbf{r}}_{\mathrm{OP}} = \begin{bmatrix} \dot{x} + \frac{\mathrm{d}}{\mathrm{d}t}\xi(x,t) \\ \frac{\mathrm{d}}{\mathrm{d}t}\eta(x,t) \\ 0 \end{bmatrix} = \begin{bmatrix} \dot{x} + \dot{\xi}(x,t) + \dot{x}\,\xi'(x,t) \\ \dot{\eta}(x,t) + \dot{x}\,\eta'(x,t) \\ 0 \end{bmatrix}, \tag{B4}$$

where the circle represents derivative in the moving frame (x, y, z), $\dot{\xi}(x,t)$ and $\dot{\eta}(x,t)$ denote partial derivatives with respect to time t, $\xi'(x,t)$ and $\eta'(x,t)$ denote partial derivatives with respect to space x, and we used the vectors $\mathbf{v}_{\mathrm{O}} = [\, v_{\mathrm{O}} \cos\alpha \;\; -v_{\mathrm{O}} \sin\alpha \;\; 0\,]^\top$, $\boldsymbol{\omega} = [\, 0 \;\; 0 \;\; \omega_z\,]^\top$ while assuming $|\mathbf{v}_{\mathrm{O}}| = v_{\mathrm{O}} > 0$. Then the velocity of point P can be obtained as:

$$\mathbf{v}_{\mathrm{P}} = \mathbf{v}_{\mathrm{P,carr}} + \mathbf{v}_{\mathrm{P,rel}} = \begin{bmatrix} -r\Omega + v_{\mathrm{O}} \cos\alpha \; - \omega_z \eta(x,t) + \dot{\xi}(x,t) - r\Omega\, \xi'(x,t) \\ -v_{\mathrm{O}} \sin\alpha + \omega_z x + \omega_z \xi(x,t) + \dot{\eta}(x,t) - r\Omega\, \eta'(x,t) \\ 0 \end{bmatrix}, \tag{B5}$$

where we used $\dot{x} = -r\Omega$, which holds since the band is unstretchable. Note that the first two terms in the first two rows of (B5) represent the velocity $\mathbf{v}_{\mathrm{Q}}$ of the point Q which is attached to the unstretchable band.

Because the time scale of the tire dynamics is generally much smaller than that of the vehicle dynamics, one may neglect the transient behavior of the tire, and consider the steady-state solution $\dot{\xi}(x,t) = 0$, $\dot{\eta}(x,t) = 0$ with assumptions $\omega_z = 0$, $\Omega = \text{const.}$, $v_{\mathrm{O}} = \text{const.}$, $\alpha = \text{const.}$. That is, we consider $\xi(x)$, $\eta(x)$. This results in

$$\mathbf{v}_{\mathrm{P}} \approx \begin{bmatrix} -r\Omega + v_{\mathrm{O}} \cos\alpha - r\Omega\, \xi'(x) \\ -v_{\mathrm{O}} \sin\alpha - r\Omega\, \eta'(x) \\ 0 \end{bmatrix}, \tag{B6}$$

where again the first two terms in the first row and the first term in the second row approximate the velocity $\mathbf{v}_{\mathrm{Q}}$ in steady state. We remark that such the steady-state assumptions are often used in dynamic situations where angular velocity components ω_z and Ω, the magnitude of the wheel center velocity v_{O} and the slip angle α change in time. We also assume that in steady state the contact patch is divided into two regions: an adhesion region of length λ and a sliding region of length $2a - \lambda$; see Figure B1. The deformations along the adhesion and sliding regions are described in the next two subsections.

B.1. Adhesion Region

In the adhesion region the friction force is large enough to ensure that point P sticks to the ground, that is,

$$\mathbf{v}_{\mathrm{P}} = \mathbf{0}\,. \tag{B7}$$

Using the steady state assumption (B6), we obtain

$$\begin{aligned}\xi'(x) &= -\frac{r\Omega - v_{\mathrm{O}}\cos\alpha}{r\Omega} := -\bar{S}_x\,,\\ \eta'(x) &= -\frac{v_{\mathrm{O}}\sin\alpha}{r\Omega} := -\bar{S}_y\,,\end{aligned} \tag{B8}$$

which are the initial definitions of the longitudinal and lateral slips $\bar{S}_x$ and $\bar{S}_y$; cf. the more general definitions (9) which will be derived further below.

Integrating (B8) with respect to x yields

$$\begin{aligned}\xi(x) &= -\bar{S}_x x + C_x\,,\\ \eta(x) &= -\bar{S}_y x + C_y\,,\end{aligned} \tag{B9}$$

where the integral constant C_x and C_y shall be obtained from the boundary conditions. Depending on the rolling direction, one shall formulate boundary conditions for the leading or for the trailing edge, where the parabolic pressure distribution (B1) reaches zero values. For forward rolling $\Omega > 0$, tire particles enter the contact patch at the leading edge with zero deformation:

$$\begin{aligned}\xi(a) &= 0\,,\\ \eta(a) &= 0\,,\end{aligned} \tag{B10}$$

which results in $C_x = \bar{S}_x a$ and $C_y = \bar{S}_y a$. On the other hand for backward rolling $\Omega < 0$, tire particles enter the contact patch at the trailing edge with zero deformation:

$$\begin{aligned}\xi(-a) &= 0\,,\\ \eta(-a) &= 0\,,\end{aligned} \tag{B11}$$

which yields $C_x = -\bar{S}_x a$, $C_y = -\bar{S}_y a$.

These results can be summarized as

$$\begin{aligned}\xi(x) &= \begin{cases}\bar{S}_x(a-x) & \text{if } \ \Omega > 0\,,\\ -\bar{S}_x(a+x) & \text{if } \ \Omega < 0\,,\end{cases}\\ \eta(x) &= \begin{cases}\bar{S}_y(a-x) & \text{if } \ \Omega > 0\,,\\ -\bar{S}_y(a+x) & \text{if } \ \Omega < 0\,.\end{cases}\end{aligned} \tag{B12}$$

This means that within the adhesion region the deformations are linear functions of x along the contact line; see Figure B1.

The longitudinal and lateral components of the tire force per unit length are denoted by f_x and f_y in the adhesion region. These can be calculated by multiplying the deformations (B12) with the distributed tire stiffnesses:

$$\begin{aligned}f_x(x) = k_x\xi(x) &= \begin{cases}k_x\bar{S}_x(a-x) & \text{if } \ \Omega > 0\,,\\ -k_x\bar{S}_x(a+x) & \text{if } \ \Omega < 0,\end{cases}\\ f_y(x) = k_y\eta(x) &= \begin{cases}k_y\bar{S}_y(a-x) & \text{if } \ \Omega > 0\,,\\ -k_y\bar{S}_y(a+x) & \text{if } \ \Omega < 0\,.\end{cases}\end{aligned} \tag{B13}$$

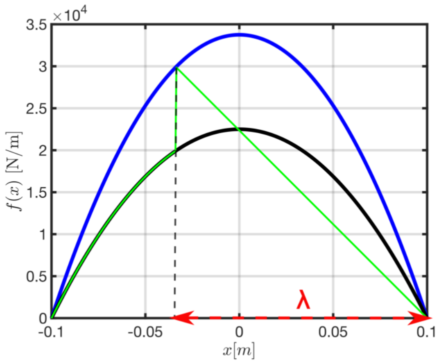

(a) Adhesion + sliding

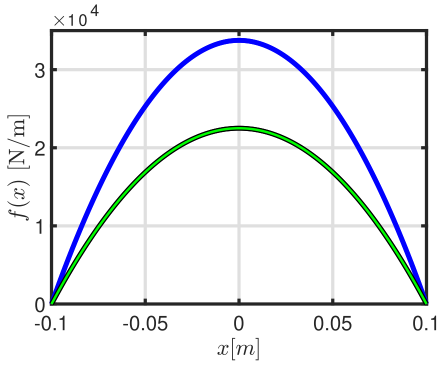

(b) Total sliding

Figure B2. Magnitude of the tire force per unit length along the contact patch for normal force $F_z = 5000\,\mathrm{N}$. The blue curves show the maximum available static friction magnitude while the black curves show the magnitude of the sliding friction. The green curves depict the change of the magnitude of the tire force (a) when adhesion occurs at the front and sliding occurs at the rear of the contact line, and (b) when sliding occurs along the whole contact line.

This means that within the adhesion region the longitudinal and lateral forces change linearly along the contact line. Consequently, the magnitude f of distributed force also follows the same trend:

$$f(x) = \sqrt{f_x^2(x) + f_y^2(x)} = \begin{cases} \sqrt{k_x^2 \bar{S}_x^2 + k_y^2 \bar{S}_y^2}\,(a-x) & \text{if } \Omega > 0\,, \\ \sqrt{k_x^2 \bar{S}_x^2 + k_y^2 \bar{S}_y^2}\,(a+x) & \text{if } \Omega < 0\,. \end{cases} \tag{B14}$$

B.2. Sliding Region

The calculations of the deformation in the adhesion region were based on the assumption that the tire particles stick to the road surface. However, when the force magnitude $f(x)$ per unit length exceeds the maximum static friction available at location x, sliding occurs for that particular brush element. Then the tire force for this brush element needs to be calculated using the sliding friction. In Figure B.2, the blue parabolas show the magnitude of the maximum available static friction force f_{stat} per unit length while the black parabolas depict the magnitude of the sliding friction force f_{slid} per unit length as a function of position x. These can be calculated as

$$f_{\mathrm{stat}}(x) = \mu_0 w\, p(x) = \frac{3\mu_0 F_z}{4a}\left(1 - \frac{x^2}{a^2}\right)\,, \tag{B15}$$

$$f_{\mathrm{slid}}(x) = \mu w\, p(x) = \frac{3\mu F_z}{4a}\left(1 - \frac{x^2}{a^2}\right)\,, \tag{B16}$$

where the expression (B1) of the pressure $p(x)$ was used. The green curve in panel (a) depicts a steady state scenario with adhesion at the front and sliding at the rear of the contact line, which occurs for forward rolling $\Omega > 0$. For backward rolling $\Omega < 0$, the force distribution would be mirrored to the vertical axis. Panel (b) shows the case when sliding occurs in the entire contact line which is often referred to as total sliding.

At the boundary of the adhesion and the sliding regions, the force magnitude f and the static friction force f_{stat} are equal; see Figure B.2(a). Let us denote the adhesion length with λ. For forward rolling ($\Omega > 0$), we have

$$f(a-\lambda) = f_{\text{stat}}(a-\lambda)\,. \tag{B17}$$

Then using (B1), (B14), (B15) with $\Omega > 0$ the adhesion length can be calculated as

$$\lambda = 2a - \frac{4a^3}{3\mu_0 F_z}\sqrt{k_x^2\bar{S}_x^2 + k_y^2\bar{S}_y^2}\,, \tag{B18}$$

cf. (16). For backward rolling ($\Omega > 0$), one shall change the argument $a-\lambda$ to $-a+\lambda$ in (B17), while (B18) still holds.

When the longitudinal slip values are large enough, the slope of the linear function (B14) reaches that of (B15). In this case the adhesion region disappears and sliding occurs along the whole contact line, cf. panels (a) and (b) in Figure B.2. For forward rolling ($\Omega > 0$), the gradients become equal at the leading edge:

$$\left.\frac{\mathrm{d}f(x)}{\mathrm{d}x}\right|_{x=a} = \left.\frac{\mathrm{d}f_{\text{stat}}(x)}{\mathrm{d}x}\right|_{x=a}. \tag{B19}$$

Substituting equations (B14) and (B15) into (B19) gives

$$k_x^2\bar{S}_x^2 + k_y^2\bar{S}_y^2 = \left(\frac{3\mu_0 F_z}{2a^2}\right)^2, \tag{B20}$$

see (18), (19) and the ellipse in Figure 6. For backward rolling ($\Omega > 0$), one shall use $x=-a$ instead of $x=a$ in (B19), but (B20) still holds.

In the sliding region, the magnitude f of the tire force per unit length is given by f_{slid} in (B16), while the longitudinal and lateral components f_x and f_y can be obtained by noticing that the direction of sliding friction force is the opposite of velocity $\mathbf{v}_{\mathrm{P}}$, cf. (B6). This contains the derivatives $\xi'(x)$ and $\eta'(x)$ which are often neglected in the literature [31]. Accordingly, we introduce the sliding velocity

$$\mathbf{v}_{\mathrm{s}} := \mathbf{v}_{\mathrm{Q}} \approx \begin{bmatrix} -r\Omega + v_{\mathrm{O}}\cos\alpha \\ -v_{\mathrm{O}}\sin\alpha \\ 0 \end{bmatrix}, \tag{B21}$$

cf. (14), to describe the direction of the tire force which does not change along the sliding region. As illustrated in Figure B1, we define the sliding angle

$$\beta = \operatorname{arctan2}(-v_{\mathrm{s},y}, -v_{\mathrm{s},x}) = \operatorname{arctan2}\left(v_{\mathrm{O}}\sin\alpha, r\Omega - v_{\mathrm{O}}\cos\alpha\right). \tag{B22}$$

cf. (15). Then, in the sliding region, the longitudinal and lateral components of the tire force per unit length can be expressed as

$$\begin{aligned} \tilde{f}_x(x) &= f_{\text{slid}}(x)\cos\beta = \frac{3\mu F_z}{4a}\left(1-\frac{x^2}{a^2}\right)\cos\beta\,, \\ \tilde{f}_y(x) &= f_{\text{slid}}(x)\sin\beta = \frac{3\mu F_z}{4a}\left(1-\frac{x^2}{a^2}\right)\sin\beta\,, \end{aligned} \tag{B23}$$

where we substituted $f_{\mathrm{slid}}(x)$ from (B16).

We remark that one may indeed obtain a more accurate expression of the force component in the sliding region by not omitting $\xi'(x)$ and $\eta'(x)$, that is, by using $\mathbf{v}_{\mathrm{P}}$ rather than $\mathbf{v}_{\mathrm{Q}}$ for the sliding velocity; cf. (B6) and (B21). In this case the sliding angle β depends on the position x according to

$$\beta(x) = \operatorname{arctan2}(-v_{\mathrm{P},y}, -v_{\mathrm{P},x}) = \operatorname{arctan2}\left(v_{\mathrm{O}}\sin\alpha + r\Omega\,\eta'(x), r\Omega - v_{\mathrm{O}}\cos\alpha + r\Omega\xi'(x)\right). \tag{B24}$$

cf. (B22). Moreover, (B23) generalizes to

$$\begin{aligned}\tilde{f}_x(x) &= f_{\mathrm{slid}}(x)\cos\beta(x)\,,\\ \tilde{f}_y(x) &= f_{\mathrm{slid}}(x)\sin\beta(x)\,.\end{aligned} \tag{B25}$$

Finally, these components can still be expressed as

$$\begin{aligned}\tilde{f}_x(x) &= k_x\xi(x)\,,\\ \tilde{f}_y(x) &= k_y\eta(x)\,,\end{aligned} \tag{B26}$$

which lead to

$$\frac{k_y\eta(x)}{k_x\xi(x)} = \frac{v_{\mathrm{O}}\sin\alpha + r\Omega\eta'(x)}{r\Omega - v_{\mathrm{O}}\cos\alpha + r\Omega\xi'(x)}\,. \tag{B27}$$

and

$$k_x^2\xi^2(x) + k_y^2\eta^2(x) = f_{\mathrm{slid}}^2(x)\,, \tag{B28}$$

whose derivative with respect to x results in

$$k_x^2\xi(x)\xi'(x) + k_y^2\eta(x)\eta'(x) = f_{\mathrm{slid}}(x)f'_{\mathrm{slid}}(x)\,. \tag{B29}$$

Solving equations (B27) and (B29) for $\xi'(x)$ and $\eta'(x)$, we obtain a dynamical system for the deformation functions in the sliding region:

$$\begin{aligned}\xi'(x) &= \frac{-\big(r\Omega - v_{\mathrm{O}}\cos\alpha\big)k_y^3\eta^2(x) + \big(v_{\mathrm{O}}\sin\alpha\big)k_xk_y^2\xi(x)\eta(x) + f_{\mathrm{slid}}(x)f'_{\mathrm{slid}}(x)r\Omega k_x\xi(x)}{r\Omega\big(k_x^3\xi^2(x) + k_y^3\eta^2(x)\big)}\,,\\ \eta'(x) &= \frac{-\big(v_{\mathrm{O}}\sin\alpha\big)k_x^3\xi^2(x) + \big(r\Omega - v_{\mathrm{O}}\cos\alpha\big)k_x^2k_y\xi(x)\eta(x) + f_{\mathrm{slid}}(x)f'_{\mathrm{slid}}(x)r\Omega k_y\eta(x)}{r\Omega\big(k_x^3\xi^2(x) + k_y^3\eta^2(x)\big)}\,.\end{aligned} \tag{B30}$$

These differential equations can be numerically solved using the boundary conditions (B10) or (B11) in order to obtain the longitudinal and lateral deformations, and via (B26) the longitudinal and lateral tire forces per unit length in the sliding region. The resultant differences in the total tire force and aligning moment between this exact solution and the approximation (B23) will be compared below.

B.3. Total Tire Force and Aligning Moment

Using the results of Sections B.1 and B.2, one can calculate the resultant of the tire force system with respect to point C, see Figure B1. Namely, the longitudinal and lateral components F_x and F_y of the total tire force can be calculated by integrating the force component acting on each brush elements in the adhesion region (cf. (B13)) and sliding region (cf. (B23)). Similarly, the aligning moment M_z (about point C) can be calculated as the integral of the moments of the lateral force components acting on the brush elements. These yield

$$
\begin{aligned}
F_x &= \begin{cases} \displaystyle\int_{a-\lambda}^{a} f_x(x)\,\mathrm{d}x + \int_{-a}^{a-\lambda} \tilde{f}_x(x)\,\mathrm{d}x & \text{if } \ \Omega > 0\,, \\ \displaystyle\int_{-a}^{-a+\lambda} f_x(x)\,\mathrm{d}x + \int_{-a+\lambda}^{a} \tilde{f}_x(x)\,\mathrm{d}x & \text{if } \ \Omega < 0\,, \end{cases} \\
F_y &= \begin{cases} \displaystyle\int_{a-\lambda}^{a} f_y(x)\,\mathrm{d}x + \int_{-a}^{a-\lambda} \tilde{f}_y(x)\,\mathrm{d}x & \text{if } \ \Omega > 0\,, \\ \displaystyle\int_{-a}^{-a+\lambda} f_y(x)\,\mathrm{d}x + \int_{-a+\lambda}^{a} \tilde{f}_y(x)\,\mathrm{d}x & \text{if } \ \Omega < 0\,, \end{cases} \\
M_z &= \begin{cases} \displaystyle\int_{a-\lambda}^{a} x f_y(x)\,\mathrm{d}x + \int_{-a}^{a-\lambda} x\tilde{f}_y(x)\,\mathrm{d}x & \text{if } \ \Omega > 0\,, \\ \displaystyle\int_{-a}^{-a+\lambda} x f_y(x)\,\mathrm{d}x + \int_{-a+\lambda}^{a} x\tilde{f}_y(x)\,\mathrm{d}x & \text{if } \ \Omega < 0\,. \end{cases}
\end{aligned}
\tag{B31}
$$

Substituting (B13) and (B23) into (B31) we obtain

$$
\begin{aligned}
F_x &= \begin{cases} \dfrac{\lambda^2}{2} k_x \bar{S}_x + \dfrac{(2a-\lambda)^2(a+\lambda)}{4a^3}\mu F_z \cos\beta & \text{if } \ \Omega > 0\,, \\ -\dfrac{\lambda^2}{2} k_x \bar{S}_x + \dfrac{(2a-\lambda)^2(a+\lambda)}{4a^3}\mu F_z \cos\beta & \text{if } \ \Omega < 0\,, \end{cases} \\
F_y &= \begin{cases} \dfrac{\lambda^2}{2} k_y \bar{S}_y + \dfrac{(2a-\lambda)^2(a+\lambda)}{4a^3}\mu F_z \sin\beta & \text{if } \ \Omega > 0\,, \\ -\dfrac{\lambda^2}{2} k_y \bar{S}_y + \dfrac{(2a-\lambda)^2(a+\lambda)}{4a^3}\mu F_z \sin\beta & \text{if } \ \Omega < 0\,, \end{cases} \\
M_z &= \begin{cases} \dfrac{(3a-2\lambda)\lambda^2}{6} k_y \bar{S}_y - \dfrac{3(2a-\lambda)^2\lambda^2}{16a^3}\mu F_z \sin\beta & \text{if } \ \Omega > 0\,, \\ -\dfrac{(3a-2\lambda)\lambda^2}{6} k_y \bar{S}_y - \dfrac{3(2a-\lambda)^2\lambda^2}{16a^3}\mu F_z \sin\beta & \text{if } \ \Omega < 0\,, \end{cases}
\end{aligned}
\tag{B32}
$$

where λ and β should be substituted from (B18) and (B22), respectively.

One may notice that in (B32) the formulae for forward rolling ($\Omega > 0$) and backward rolling ($\Omega < 0$) are almost identical, apart from a few sign changes. This motivates us to re-define the lateral and longitusinal slips as

$$
\begin{aligned}
S_x &:= \frac{r\Omega - v_{\mathrm{O}}\cos\alpha}{|r\Omega|}\,, \\
S_y &:= \frac{v_{\mathrm{O}}\sin\alpha}{|r\Omega|}\,.
\end{aligned}
\tag{B33}
$$

cf. (B8) and (9). This way the expressions of the forces and aligning moment can be simplified to

$$
\begin{aligned}
F_x &= \frac{\lambda^2}{2} k_x S_x + \frac{(2a-\lambda)^2(a+\lambda)}{4a^3} \mu F_z \cos\beta \,, \\
F_y &= \frac{\lambda^2}{2} k_y S_y + \frac{(2a-\lambda)^2(a+\lambda)}{4a^3} \mu F_z \sin\beta \,, \\
M_z &= \frac{(3a-2\lambda)\lambda^2}{6} k_y S_y - \frac{3(2a-\lambda)^2\lambda^2}{16a^3} \mu F_z \sin\beta \,.
\end{aligned}
\tag{B34}
$$

Moreover, using the slip definitions (B33), one may obtain

$$
\lambda = 2a - \frac{4a^3}{3\mu_0 F_z} \sqrt{k_x^2 S_x^2 + k_y^2 S_y^2} \,,
\tag{B35}
$$

cf. (16) and (B18), and

$$
\begin{aligned}
\cos\beta &= \frac{S_x}{\sqrt{{S_x}^2 + {S_y}^2}} \,, \\
\sin\beta &= \frac{S_y}{\sqrt{{S_x}^2 + {S_y}^2}} \,,
\end{aligned}
\tag{B36}
$$

cf. (15) and (B22), which can be directly substituted into (B34). Thus, the tire force component and the aligning moment can be expressed as the explicit function of the longitudinal and lateral slips S_x and S_y.

Indeed, (B34) is only valid when there exist an adhesion region along the contact line, that is when (18) hold. When sliding occurs along the entire contact line, that is for (19), the total tire force and aligning moment should be calculated via

$$
\begin{aligned}
F_x &= \int_{-a}^{a} \tilde{f}_x(x)\,\mathrm{d}x \,, \\
F_y &= \int_{-a}^{a} \tilde{f}_y(x)\,\mathrm{d}x \,, \\
M_z &= \int_{-a}^{a} x\tilde{f}_y(x)\,\mathrm{d}x \,,
\end{aligned}
\tag{B37}
$$

instead of (B31). Then, using (B23) results in

$$
\begin{aligned}
F_x &= \mu F_z \cos\beta \,, \\
F_y &= \mu F_z \sin\beta \,, \\
M_z &= 0 \,.
\end{aligned}
\tag{B38}
$$

Combining (B34) and (B38) we obtain (20).

We emphasize again that, besides the steady-state assumption, these analytical results were obtained with an approximation which uses the velocity of point Q rather than that of point P as the sliding velocity; cf. (B21) and (B6). Without this approximation, the deformations $\xi(x)$ and $\eta(x)$ in the sliding region should be derived by solving the differential equation (B30) numerically with boundary conditions (B10)

Table B1. Differences between analytical approximation and the numerical computation of the tire force components and aligning moments for specific slip values and normal force $F_z = 5000\,\mathrm{N}$ with the other parameters selected from Table 1

$S_x = 0.0474,\ S_y = 0.0525\ [S_x \approx S_y]$	Analytical approximation	Numerical
ΔF_x [N]	2332	2427
ΔF_y [N]	1438	1235
ΔM_z [Nm]	−21.54	−15.53

$S_x = 0.0474,\ S_y = 0.2522\ [S_x \ll S_y]$	Analytical approximation	Numerical
ΔF_x [N]	689	735
ΔF_y [N]	3038	3027
ΔM_z [Nm]	6.89	15.59

$S_x = 0.1374,\ S_y = 0.0470\ [S_x \gg S_y]$	Analytical approximation	Numerical
ΔF_x [N]	2914	2999
ΔF_y [N]	991	755
ΔM_z [Nm]	1.41	1.15

or (B11). Here, by comparing the analytical approximation to the exact numerical results, we show that the approximation does not alter the tire force significantly but may impact the aligning moment.

Considering forward rolling ($\Omega > 0$), we solve the ordinary differential equation (B30) with boundary condition (B10) for different (S_x, S_y) pairs. In particular, we fix the angular speed Ω of the wheel and vary the speed v_{O} of the wheel center and the slip angle α. After obtaining $\xi(x)$ and $\eta(x)$ numerically in the sliding region, and still analytically as $\xi(x) = S_x(a-x)$ and $\eta(x) = S_y(a-x)$ in the adhesion region (see (B12)), we calculate tire force per unit length as (B13). Then, we obtain the total tire force and aligning moment by numerical integration along the contact patch using (B31) (when there exist an adhesion region) or (B37) (when sliding occurs along the entire contact line). Table B1 showcases the differences between the analytical approximation and the numerical computation for three different scenarios $S_x \approx S_y$, $S_x \ll S_y$, and $S_x \gg S_y$. The differences for the force components are consistently small while those for the aligning moments can be relatively significant.

Figure B.3 compares the analytical approximation with the numerical computation in the domain ($S_x \in [-0.5, 0.5], S_y \in [-0.5, 0.5]$); cf. Figure 7. Clearly the differences in the force components are not significant; the maximum difference in Figure B.3(b),(d) is around 300 N, while the maximum value in Figure 7(b),(d) is around 3500 N. On the other hand, the difference in the aligning moment is more pronounced; the maximum difference in Figure B.3(f) is around 15 [Nm] while the maximum value in Figure 7(f) is around 35 N. In the models (1) and (7) used in this paper, the torque error introduced by the approximation is still negligible since the aligning moments are themselves negligible compared to the torques of the lateral tire forces, which are in the order of 1000 [Nm].

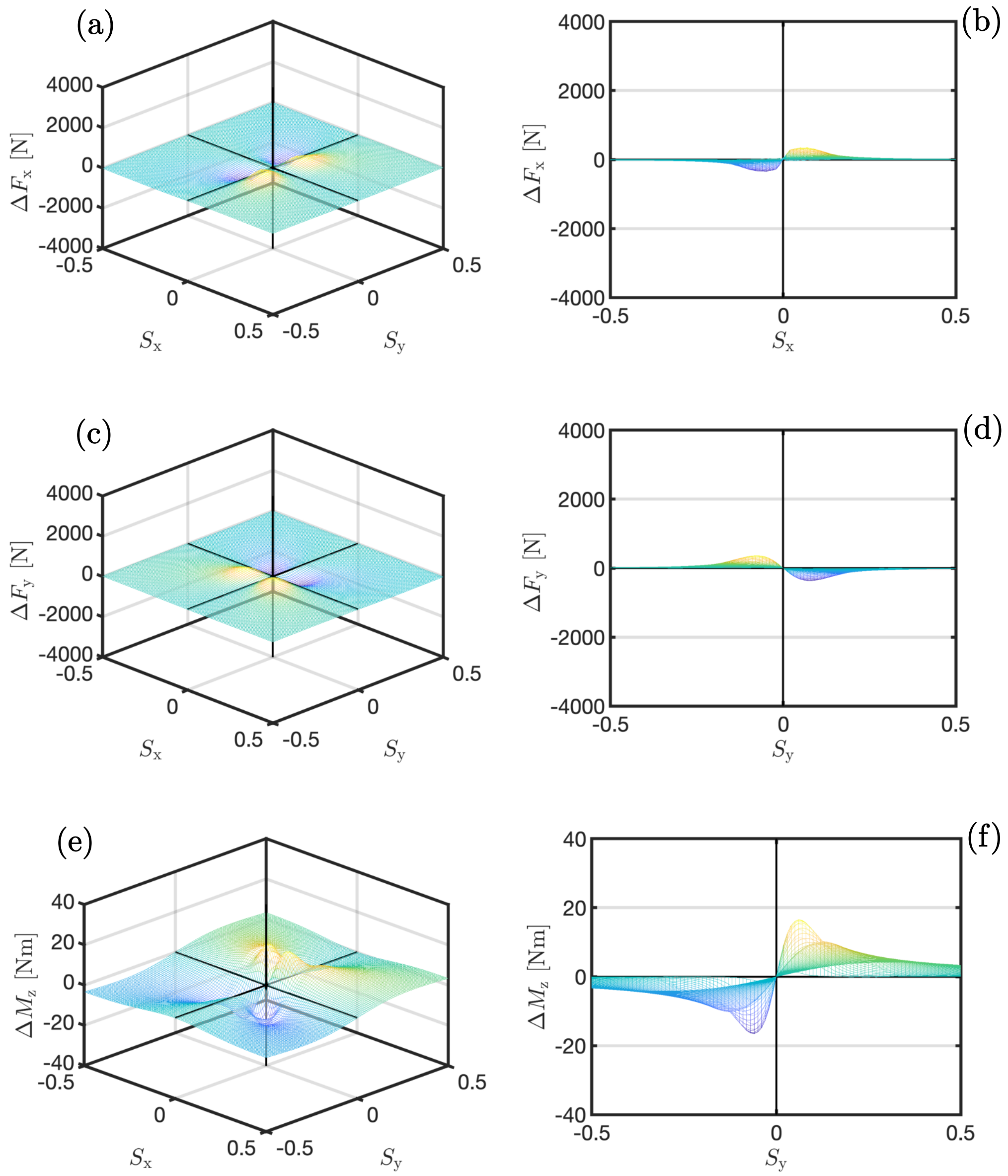

Figure B3. Differences between analytical approximation and the numerical computation for the longitudinal force F_x (a)-(b), the lateral force F_y (c)-(d), and the aligning moment M_z (e)-(f) as functions of the lateral slip S_x and longitudinal slip S_y for normal force $F_z = 5000\,\mathrm{N}$ with the other parameters selected from Table 1

In other applications (e.g., steering dynamics) the error introduced by the approximation may still be significant. For example, the approximation (B38) gives zero aligning moment when sliding occurs in the entire contact line; see Figure 7(e),(f). However, Figure B.3(e),(f) shows that this does not hold for the (more accurate) numerical results. To illuminate the reason behind this discrepancy, in Figure B4 we compare the lateral force distribution along the contact line given by the analytical approximation and the numerical computation for a specific slip combination. Under the analytic approximation the lateral force profile is a precise parabola (see (B23)), which is symmetric to the vertical axis, while the numerically obtained profile is slightly asymmetric. The areas under the two curves, i.e., the total lateral tire force F_y, is al-

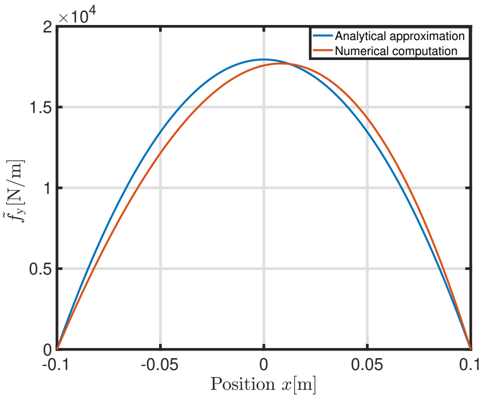

Figure B4. Lateral force distribution for slip values ($S_x = 0.1374, S_y = 0.1979$) which result in sliding along the entire contact line. The normal force $F_z = 5000\,\mathrm{N}$ and the parameters from Table 1 are used.

most the same. The aligning moment M_z, on the other hand, is only zero for the symmetric case and nonzero for the asymmetric one.